Estimating Maximum Extent of Auroral Equatorward Boundary using Historical and Simulated Surface Magnetic Field Data

Seán P. Blake[1,2], Antti Pulkkinen[2], Peter W. Schuck[2], Alex Glocer[2], Gabor Tóth[3]

The maximum extent of the auroral equatorward boundary was estimated for individual days for three decades of ground magnetic field data.

Geomagnetic storms were simulated using the Space Weather Modeling Framework, and found to give boundaries similar to historical data.

Extreme geomagnetic storms (Dst < -1000 nT) were simulated, resulting in auroral equatorward boundaries below 40° magnetic latitude.

Corresponding author: Seán P. Blake, NASA Goddard Space Flight Center, Heliophysics Science Division, USA (sean.blake@nasa.gov)

[1]Department of Physics, Catholic

Abstract. The equatorward extent of the auroral oval, the region which separates the open-field polar cap regions with the closed field subauroral regions, is an important factor to take into account when assessing the risk posed by space weather to ground infrastructure. During storms, the auroral oval is known to move equatorward, accompanied by ionospheric current systems and significant magnetic field variations. Here we outline a simple algorithm which can be used to estimate the maximum extent of the auroral equatorward boundary (MEAEB) using magnetic field data from ground-based observatories. We apply this algorithm to three decades of INTERMAGNET data, and show how the auroral oval in the Northern hemisphere moves South with larger (more negative Dst) storms. We simulate a number of storms with different magnitudes using the Space Weather Modelling Framework (SWMF), and apply the same auroral boundary detection algorithm. For SWMF simulated storms with Dst > -600 nT, the estimates

University of America, Washington, District of Columbia, USA

[2]NASA Goddard Space Flight Center, Heliophysics Science Division, Greenbelt, Maryland, USA

[3]University of michigan, Ann Arbor, MI 48109, USA

of the MEAEB are broadly in line with the same estimates for historical events. For the extreme scaled storms (with Dst< -1000 nT), there is considerable scatter in the estimated location of the auroral equatorward boundary. Our largest storm simulation was calculated using Carrington-like estimates for the solar wind conditions. This resulted in a minimum Dst $= -1142$ nT, and a minimum estimated auroral boundary of 35.5° MLAT in places.

1. Introduction

As the solar wind impacts upon the Earth's magnetosphere-ionosphere system, energy and particles are deposited into the polar regions along field lines, leading to enhanced electric currents in the ionosphere, as well as visible auroral emissions [*Buonsanto*, 1999; *Russell et al.*, 2016]. The auroral ovals are the regions centered around the geomagnetic poles that separate the Earth's closed and open magnetic field line regions. The area equatorward of the auroral ovals has closed magnetic field lines that reconnect in the opposite hemisphere, whereas the regions poleward of the auroral ovals (or polar cap regions) have open magnetic field lines that connect directly to the solar wind. The enhanced electric currents in the polar cap regions lead to elevated geomagnetic variations during geomagnetic storms. These magnetic variations are known to have an adverse effect on technologies such as pipelines [*Pirjola et al.*, 1999], railways [*Eroshenko et al.*, 2010] and most significantly, power networks [*Pulkkinen et al.*, 2017]. While geomagnetic variations occur at all latitudes, the largest variations are seen at higher latitudes, corresponding to the complicated current systems in the polar ionosphere [*Pirjola*, 2001].

During geomagnetic storms, the polar cap can expand and move equatorward, accompanied by ionospheric currents which drive surface magnetic field variations. During particularly large geomagnetic storms, the polar cap regions move into what can normally be considered subauroral latitudes under quiet conditions [*Yokoyama et al.*, 1997], leading to larger geomagnetic variations at lower latitudes. The maximum extent of the auroral equatorward boundary is therefore important to consider when assessing the risk posed by large-but-infrequent geomagnetic storms to large-scale grounded infrastructure.

A common measure of the strength of a storm is the disturbance storm-time index (Dst). This index, which has been definitively measured since 1957, is a proxy measurement of the strength of the ring current. It is derived from horizontal magnetic field measurements at four low-latitude geomagnetic observatories [*Love & Gannon*, 2009]. Since the hourly Dst has been calculated, the largest geomagnetic storm on record is the March 1989 event, with a minimum Dst = −589 nT. This storm famously precipitated the collapse of the Hydro-Quebec power system [*Bolduc*, 2002]. The large geomagnetic variations measured at mid- and high-latitudes during this storm, as well as the unusually low latitude visible aurora (seen as far South as Florida [*Allen et al.*, 1989]), indicate that the auroral oval had expanded significantly towards the equator.

While the March 1989 storm is the largest storm for which we have widespread measurements, more intense storms have likely occurred in the past. These include the May 1921 storm, which was recently estimated to have a Dst = −921 nT [*Love*, 2019]. That storm produced significant technological effects in New York (40.7° North), as well as aurora seen on the poleward horizon as far South as 30° MLAT[*Silverman & Cliver*, 2001]. The August-September 1859 'Carrington' event storm was probably even more intense, with an estimated Dst around −900 nT [*Cliver & Dietrich*, 2013]. This storm had auroral sightings reported as far South as the Carribean Sea, among other places [*Silverman*, 2005; *Hayakawa et al.*, 2016, 2018]. In addition to the extremely low-latitude auroral sightings, there was an estimated 3,000 nT deviation in the horizontal magnetic field measured at Rome. This measurement has been found to be consistent with a site within the auroral zone during recent large geomagnetic storms, and is evidence for an expanded auroral oval to at least 38.6° magnetic North during the morning of 2 September 1859 [*Blake et al.*, 2020].

A number of related but different phenomena have been used to estimate the the poleward and equatorward boundaries of the auroral oval during geomagnetic storms. These include the presence of electron precipitation [*Ngwira et al.*, 2013b; *Carbary et al.*, 2003], optical auroral sightings [*Silverman*, 2005; *Milan et al.*, 2009; *Ding et al.*, 2017], and changes in ground magnetic variations (as described above) [*Woodroffe*, 2016]. Of these different metrics, optical auroral sightings have been recorded for the longest time [*Stephenson et al.*, 2004], but it can be difficult to precisely quantify the 'footprint' location of the aurora (i.e., the locations directly beneath the aurora), and care must be taken when interpreting historical sources. In addition, auroral emissions are not always coincident with the auroral oval, and can even occur during periods of low activity [*Silverman*, 2003]. Electron precipitation data only exists for the satellite era, and as an incomplete record, so few of the largest geomagnetic storms in the record have such data.

Enhanced geomagnetic variations due to increased electric currents in the ionosphere are perhaps the most consequential indicator of the auroral boundary in terms of threats to modern infrastructure. In addition, geomagnetic data have been continuously measured across the globe since the 1830s [*Stern*, 2002], and multiple large geomagnetic storms have occurred during this time. Despite this, early geomagnetic records are often off-scale or incomplete [*Shea & Smart*, 2006], or difficult to access for performing a global study. In terms of widespread and readily accessible geomagnetic field data, digital archives such as INTERMAGNET and SuperMag host data from geomagnetic observatories from around the 1980s to present (at cadences of 1 minute or quicker).

In this paper, we outline a simple algorithm that uses only geomagnetic field data such as these from multiple locations to estimate the maximum extent of the auroral equatorward boundary (hereafter MEAEB for brevity). This algorithm separates the more equatorward and less active subauroral region from the more active poleward region in the Northern hemisphere (in terms of geomagnetic activity) for different days. We apply this algorithm to 25 years of global geomagnetic field data, and plot the location of the MEAEB against minimum Dst for each day, allowing us to build a relation between the MEAEB and storm-intensity. Finally, to investigate the MEAEB for storms larger than -589 nT, we simulate storms with a range of intensities using the Space Weather Modeling Framework (SWMF) [*Toth et al.*, 2005, 2012]. The most intense of these simulations use solar wind inputs that are scaled to Carrington-like conditions, and result in extreme geomagnetic conditions (Dst $< -1,000$ nT). We apply our auroral boundary algorithm to these simulations, and compare to estimates for the historical Carrington event.

2. Identifying MEAEB from Geomagnetic Data

The basic function of our algorithm used to calculate the MEAEB latitude is to automatedly separate the relatively geomagnetically quiet and more equatorward subauroral region from the more active poleward region, for a fixed time-period. In effect, this estimates the maximum equatorward extent of the auroral region, as opposed to an instantaneous position. The top panel of Figure 1 shows the measured horizontal magnetic field components (B_X and B_Y) for the Eskdalemuir INTERMAGNET observatory for the 29-31 October 2003 ‘Halloween’ storm period. From these, horizontal electric field values were calculated for each site using the frequency dependent (ω) plane-wave equation [*Pirjola*, 2001]:

$$\mathbf{E}(\omega) = \mathbf{Z}(\omega)\mathbf{B}(\omega) \tag{1}$$

where **E** and **B** are the electric and magnetic fields, and **Z** is the magnetotelluric or impedance tensor [*Pirjola*, 2001]. In practice, a magnetic field time-series is Fourier transformed and used in Equation 1 to get $\mathbf{E}(\omega)$, which is then inverse Fourier transformed back to a time-series. The tensor **Z** is dependent on the resistivity structure at a location. For a 1-dimensional Earth resistivity structure (i.e., where the resistivity changes only with depth), the diagonal components of **Z** are set to zero, and the electric field components can be written as

$$E_X(\omega) = \frac{1}{\mu_0} Z_{XY}(\omega) B_Y(\omega) \tag{2}$$

and

$$E_Y(\omega) = -\frac{1}{\mu_0} Z_{XY}(\omega) B_X(\omega) \tag{3}$$

where μ_0 is the vacuum permeability and subscripts X and Y refer to the North-South and East-West components, respectively. From these two calculated electric field components, the horizontal electric field (E_H) was calculated

$$E_H = \sqrt{E_X^2 + E_Y^2} \tag{4}$$

From this, the maximum E_H was noted. In this paper, the Quebec 1D resistive model outlined in *Boteler & Pirjola* [1998] was used for all electric field calculations. In reality, each of the INTERMAGNET sites will have different subsurface resistivity profiles. By using the same profile for each, we are in effect using the maximum calculated electric field value as a proxy for variations in the geomagnetic field measured at each site. This approach (using maximum 1-D calculated E_H as a proxy for magnetic variations) has been used before by *Woodroffe* [2016]; *Ngwira et al.* [2013, b], and *Pulkkinen et al.* [2015].

In addition to the maximum horizontal electric field, the magnetic latitude of the site was calculated using the AAGCMv2 method [*Shepherd*, 2014]. In the case of Eskdalemuir, this is 57.8°. For the same time-period, maximum calculated E_H values and magnetic latitudes were calculated for all available observatories (as with Eskdalemuir). A plot of E_H^{max} versus MLAT can be seen in Figure 2. For this particular example, there is a clear boundary at approximately ±50° which separates the quieter subauroral region (with calculated electric fields < 0.5 Vkm^{-1}), and the more geomagnetically active poleward regions (> 0.5 Vkm^{-1}). This boundary is what we describe as the MEAEB for this particular day, and what our algorithm attempts to identify.

In order to automatically calculate the maximum latitudinal extent of this boundary, the following steps were taken. Firstly, the logs of the maximum calculated electric field values were taken for the northern hemisphere (as there are far more points here than in the Southern hemisphere). A natural cubic spline fit was applied to the data [*Woltring*, 1986]. A fixed smoothing parameter ($p = 400$) was used in order to prevent over-fitting the data. The gradient of this smoothed fit was then taken at every point. The latitude at which this gradient was at its greatest was taken as the MEAEB location, i.e., where the amplitude of the electric field was seen to increase the most. In order to estimate errors in this fit, 500 spline fits were calculated from n randomly selected subsamples of the data (where $n = 0.75$ times the available sites). The standard deviation of these 500 calculated MEAEB locations was then used as an estimated error for the fit.

Figure 3 shows the magnetic latitude versus the $\log_{10}$ of E_H plot for a disturbed day (30 October 2003, minimum Dst = -383 nT), and a quiet day (07 October 2009, minimum Dst = 0 nT). It can be seen that the disturbed day (in blue) had elevated maximum E_H values at all latitudes when compared to the quiet day (in red). The fitted smoothed spline fits are shown as bold lines, and the vertical dashed lines show the points along these smoothed lines with the largest gradient. These mark the calculated MEAEBs for the two days. It can be seen that the disturbed day had a calculated MEAEB that occurred at 52.5°N. This value can be compared to the ±50° boundary estimated by eye in Figure 2. The quiet day's boundary was calculated at 63.7°.

2.1. Applying Algorithm to 25 Years of Geomagnetic Data

The MEAEB location was calculated for every day from 1991 to 2016 using 1-minute INTERMAGNET data taken from all available observatories. The magnetic observatories that contribute to these networks are distributed across the globe, with the majority in the northern hemisphere. Since 1991 (the start of the availability of INTERMAGNET data), the number of recording INTERMAGNET observatories has steadily increased from around 40 to over 100. In addition to the INTERMAGNET data, 1-minute data were taken from the SuperMag database (http://supermag.jhuapl.edu) for the 13-14 March 1989 geomagnetic storm.

The location and shape of the auroral oval can change significantly throughout the course of a single geomagnetic storm. The algorithm uses the maximum E_H over a fixed time-period, therefore calculating the maximum equatorward extent of the auroral boundary, as opposed to an instantaneous position. By using the maximum E_H for a relatively long period (i.e., 24 hours), the auroral and sub-auroral regions are better differentiated, as not all observatories North of the auroral boundary will experience elevated geomagnetic activity at exactly the same time. In addition, a calendar day is a convenient time window given the long timescale of 25 years covered in the study, and the fact that INTERMAGNET data files are given for individual observatories for each calendar day.

For a given day, the horizontal magnetic time-series for each available magnetic observatory were examined. Datapoints which were more than 12σ from the mean of the time-series were considered spurious and removed. Gaps in the data were linearly interpolated over. Where some time-series exhibited large artificial steps of several hundred nT (i.e., where the data baseline suddenly increased or decreased), these datasets were discarded. Using the remaining data from the observatories, the algorithm outlined in Section 2 was applied, and the MEAEB was calculated.

For each day, the calculated MEAEB was plot against the corresponding minimum daily Dst (taken from the World Data Center for Geomagnetism, Kyoto- wdc.kugi.kyoto-u.ac.jp). This can be seen in Figure 4. Errorbars are the previously mentioned $1\,\sigma$ estimates from 500 bootstrapped spline fits. As can be seen from this plot, the calculated MEAEB can be seen further South for larger geomagnetic storms. For minimum Dst values > -200 nT, days appear to have calculated MEAEB's within a decreasing band of approximately 8°. Days with minimum Dst < -200 nT are less plentiful, and show a larger scatter in MEAEB position. The day with the lowest calculated MEAEB was for the 14 March 1989, with a calculated boundary location of $45 \pm 3.8°$ magnetic latitude.

For days with low geomagnetic activity, the subauroral and poleward regions are poorly differentiated in ground geomagnetic data (or in maximum calculated E_H, our chosen proxy). As such, the boundary calculation routine outlined above can misattribute a lower auroral boundary than is expected, and produce a large $1\,\sigma$ errorbar. Figure 4 has days with $1\,\sigma > 5°$ omitted for this reason.

As previously mentioned, the number of INTERMAGNET observatories varies by date. The limited number of operational observatories towards the start of the dataset meant that binning the observatories by longitude and calculating the MEAEB for different longitudes was not possible using the above method. For example, in 1991 there were only 40 geomagnetic observatories with available data, 34 of which were in the Northern hemisphere. Furthermore, most of these were clustered around Europe. All available INTERMAGNET data were therefore used for every day, and a single latitude value was returned for the MEAEB.

In order to investigate how the number of available observatories affects the calculated MEAEB location, two storm events with a large number of recording observatories were chosen. These were the 30 October 2003 and 17 March 2015 events. For both storm events, an increasing number of observatories (from 40 to the maximum number available) were chosen at random, and the MEAEB was calculated. This was repeated 1,000 times to get 90% confidence intervals for the boundary calculations, for every number of available magnetic observatories.

Figure 5 shows the mean of the calculated MEAEBs for both events, as well as the 90% confidence intervals. For both, as the number of observatories used in the boundary calculation increases, the 90% intervals narrow. In the case of the 30 October 2003 event, the mean MEAEB only changes by a fraction of a degree as the number of sites is increased from 40 to 90. For the 17 March 2015 event, the mean MEAEB changes by approximately 1.7° as the number of observatories is increased from 40 to 113. The difference between the change in MEAEB for the two storms may be due to intensity or global structure of the individual storms. For both events, the calculated MEAEB using all available sites was within the 90% confidence interval for the calculated MEAEB using only 40 sites. From these two events, we conclude that days with more available magnetic observatories will have smaller uncertainties associated with the MEAEB calculation. In addition, there is an uncertainty on the order of a few degrees in the location of the calculated MEAEB using our algorithm.

3. SWMF Simulations and Setup

The simulations performed in this paper use the Space Weather Modelling Framework (SWMF), a software framework for physics based simulations of the Sun-Earth system [*Toth et al.*, 2005, 2012]. The SWMF combines a number of different physics domains that span a wide range of spatial and temporal scales. These domains cover different parts of the Sun-Earth environment, from the solar corona to the ionosphere. The model used in this study consists of the Block-Adaptive Tree Solar wind Roe-type Upwind Scheme global magnetosphere model (BATS-R-US) coupled to the Rice Convection Model for the inner magnetosphere (RCM) and the Ridley Ionosphere Model (RIM), which together simulate the magnetosphere-ionosphere system's interaction for a number of different solar wind driver scenarios.

BATS-R-US is a magnetohydrodynamic (MHD) model which simulates the plasma conditions in the magnetosphere on a block-adaptive grid [*Powell et al.*, 1999; *De Zeeuw et* *al.*, 2000]. RCM models the inner magnetosphere [*Toffoletto et al.*, 2003; *De Zeeuw et al.*, 2004], capturing ring current dynamics by receiving magnetic field and plasma moments from BATS-R-US, then returning plasma density and pressure back to BATS-R-US. RIM is a height-integrated ionospheric electrodynamics model [*Ridley et al.*, 2004]. It receives field-aligned current density from BATS-R-US, and delivers electric potential to RCM and BATS-R-US. The communication among these models is facilitated by the SWMF, allowing for a more comprehensive representation of the Earth's magnetosphere-ionosphere system.

Surface magnetic field perturbations are calculated as part of the SWMF on a user-defined grid for a specified timestep. The surface magnetic field at any point is approximately the sum of the Biot-Savart integrals calculated magnetic contributions from each of the current systems in the magnetospheric and ionospheric domain, as well as the field-aligned currents which connect them. The simulations in this study output a $1 \times 1°$ grid every 60s. In addition, the simulations output magnetospheric conditions, a 2d shell of ionospheric currents and a SYM-H estimate from the simulation, which is in effect a 1-minute Dst value [*Wanliss & Showalter*, 2006].

The combination of BATS-R-US, RIM and RCM is well established for extreme geomagnetic storm simulations [*Ngwira et al.*, 2013, 2014; *Welling*, 2020], and has been shown to perform well when replicating surface dB/dt [*Pulkkinen et al.*, 2013; *Toth et al.*, 2014] and Dst. It is currently being used for operational forecasting at the Space Weather Prediction Center [*Haiducek et al.*, 2017].

Each of the simulations in this paper was run on a grid made up of approximately 5.89 million computational cells, with the smallest cells being 1/16 Earth radii in size. A high coupling rate of 5 s was chosen for the different modules, and $F_{10.7}$ value of 275 solar flux units was used. This value is consistent with solar maximum conditions [*Ngwira et al.*, 2014]. Typically in SWMF simulations, the inner magnetosphere boundary (R_{body}) and location at which the magnetospheric currents are mapped (R_{curr}) are set to 2.5 and 3.0 R_E respectively. Despite requiring greater computational time, we found that when attempting to simulate larger geomagnetic storms, smaller values for these numbers were necessary in order to correctly map geomagnetic variations at lower latitudes. This is explored further in Appendix A. We therefore reduced these values, depending on the severity of the solar wind drivers used as inputs. For our largest storm simulations, we set $R_{body} = 1.25\,R_E$ and $R_{curr} = 1.5\,R_E$. The latitudinal resolution for RIM was 1°, and the latitude boundary for RIM was 10°. For all the simulations performed in this study, the radial magnetic field was not forced to coincide with the internal magnetic field ($B0$ value in the simulations). Due to this smaller boundary in the simulation, we also increased the particle density at the magnetospheric boundary to 1,000 particles cm^{-3}.

3.1. Solar Wind Scenarios

Inputs for the simulations are solar wind components in the form of magnetic field, velocity, temperature and density. For our simulations, 1-min data were taken from the ACE and WIND spacecraft (accessed via NASA's OMNIWeb portal - omniweb.gsfc.nasa.gov). Seven periods with different solar wind conditions were chosen to be simulated. These periods were chosen according to solar wind data availability, and because these periods had a range of actual Dst values, from very quiet (Dst= 0 nT) to extremely disturbed (Dst= −422 nT). The solar wind conditions, actual measured minimum Dst values and simulated minimum Dst values are shown in Table 1.

Solar wind data are of limited availability (due to saturation of satellite instruments during large events), so in order to simulate extreme events more intense than March 1989 event (Dst < -589 nT), the solar wind conditions during two recent storms were scaled and used as inputs for the SWMF simulations. The two storms chosen were the 20-21 November 2003 storm (with a minimum Dst$= -422$ nT), and the 8-9 November 2004 storm (minimum Dst$= -374$ nT). This scaling approach was chosen in order to maintain some small-scale structure within the solar wind, as opposed to creating completely synthetic time-series.

The velocity, magnetic field, density and temperatures for the unscaled November 2003 event are shown in Figure 6. An hour into the time-series (dashed vertical red line) marks the arrival for the CME for this storm. Each of time-series after this point were scaled by some factor, to get different solar wind scenarios of increasing intensity. The final scaled iteration (Scaled-B6 in Table 1) is what we estimate to be a 'Carrington-like' storm.

For our Carrington event, a maximum estimated velocity of 1,945 kms^{-1} was chosen. This approximate value was arrived at by comparing the timing of the flare on 1 September 1859, with the onset of the geomagnetic storm on the 2 September 1859 [*Cliver & Dietrich*, 2013; *Li et al.*, 2006]. *Manchester et al.* [2005] simulated an extremely fast CME which travelled 1 AU in 18 hours (approximately the same time as the Carrington CME). In order to achieve this, their simulated CME had an eruptive velocity of 4,000 kms^{-1}. This reduced to $\sim 2,000$ kms^{-1} at 1 AU. For our Carrington-like solar wind conditions, the velocity after 0801 UT was therefore multiplied by 2.59. Of all of the components of the solar wind, the velocity is the only value that we can bound with some confidence for the Carrington event. Other values must be inferred, or arbitrarily scaled. A maximum intensity for the total magnetic field of the solar wind inputs was set at 91 nT. This value is calculated from the empirical relationship between velocity and B of magnetic clouds at 1 AU recorded by *Gonzalez et al.* [1998]:

$$B_{peak}(\mathrm{nT}) = 0.047 \times V_{peak}(\mathrm{kms}^{-1}) \tag{5}$$

Although we note here that this relationship is derived from a limited CME dataset with peak B intensities of < 40 nT. The B_y and B_z components of our solar wind were therefore scaled by a factor of 1.6 after 0801 UT. The density was multiplied by a factor of 4 so that it peaked with 115 cm^{-3}. This arbitrary multiplier is large, but we note that it results in a time-series with a lower peak density than has been measured before in CMEs [*Tsurutani et al.*, 2003]. Finally, the temperature was multiplied by a factor of 8, to give a maximum of 6 MK. This is in line with the measured temperature of the July 2012 fast CME [*Ngwira et al.*, 2013]. With these solar wind inputs, the Carrington-like simulation returned a minimum Dst of -1142 nT. This value is in the upper range of Dst estimates for the Carrington event derived using historical magnetic field data(see *Cliver & Dietrich* [2013] and references within).

The 20-21 November 2003 solar wind conditions were incrementally scaled six times, to get six different storm events with decreasing Dst (increasing intensity). The 8-9 November 2004 conditions were scaled only twice, as it was found that even when scaled to Carrington-like conditions (Scaled-A2 in Table 1), this resulted in a minimum Dst of only -757 nT.

4. Calculating MEAEB from SWMF Ground Magnetics

As mentioned above, the SWMF simulations can calculate the geomagnetic field for a user specified grid. In our case, the simulations calculated geomagnetic field data on a $1 \times 1^{\circ}$ grid in geomagnetic coordinates. We can therefore apply our auroral boundary algorithm to the SWMF simulated geomagnetic data in different ways. Here we outline two approaches. Firstly, we interpolate the geomagnetic field data to INTERMAGNET locations in order to directly compare with our historical MEAEB estimates. Secondly, we use all of the available simulated geomagnetic data to get a 2D estimate of the MEAEB.

4.1. Method 1: Interpolating to INTERMAGNET sites

In order to directly compare the simulation outputs with the MEAEB locations calculated from INTERMAGNET data, the simulated geomagnetic field outputs were interpolated to the magnetic coordinates for all of the 95 INTERMAGNET stations that were recording in 2017. From these, E_H was calculated using the Quebec resistivity model as before. Then our boundary algorithm was applied. The normalized electric fields in the Northern hemisphere and resulting calculated boundaries for 12 of the simulations are shown in Figure 7. This shows the location of the INTERMAGNET sites as white dots, the calculated boundary as a horizontal red line, and bootstrapped 1σ estimates as a yellow horizontal region.

The daily minimum Dst versus calculated MEAEB latitudes are shown in the top panel of Figure 8 for both the historical INTERMAGNET data and each of the SWMF simulations (as red stars). For storms with Dst $>$ -600 nT, the calculated MEAEB location/minimum Dst pairs for the simulations appear to line up quite well with the historical data, indicating that for storms of this magnitude, the SWMF can reproduce the maximum extent of the auroral boundary. Beyond -600 nT, the simulated points become more scattered. Of the most intense storms (< -1000 nT Dst), the minimum calculated auroral boundary location was 40.87° ± 1.59° MLAT. The black line shows the simple empirical fit that was applied to the simulated auroral boundary locations. This relation between auroral boundary locations and Dst takes the form

$$\text{Boundary (MLAT)} = 36.7 - \frac{9,400}{\text{Dst} - 342}, \qquad (-1150 < \text{Dst} < 0 \text{ nT}) \tag{6}$$

The shaded black region shows a fit of the same form applied to the calculated boundaries $\pm 2\sigma$.

4.2. Method 2: Using all Simulated Geomagnetic field Data

The second approach used all the simulated geomagnetic field to calculate the MEAEB location. For each simulation, the maximum electric field was calculated at all points of the output grid. For every line of longitude, a ±10° averaging window was applied to the maximum calculated E_H for each latitude bin. The boundary algorithm was then applied to the resulting averaged geoelectric field to get an auroral boundary location estimate for that particular line of longitude. The window was moved longitudinally by a 1° increment and the process was repeated in order to get a 360° estimate of the auroral boundary location.

Figure 9 shows the location of these calculated auroral boundaries for 12 of the simulations. The calculated MEAEBs can be seen to move South as the simulated storm intensities increases. The calculated MEAEBs generally separate the Northerly active regions from the quieter Southerly regions well. Exceptions to this are the two lowest intensity storm simulations (Dst -1 and -7 nT). In these examples, the algorithm does not perform well, for the same reason that it does not perform well for quiet historical days; subauroral and poleward regions are poorly differentiated in terms of E_H amplitudes. In addition, for the most intense simulations (Dst < -1000 nT), the auroral boundary estimate is discontinuous in places.

For every simulation, there are therefore 360 calculated MEAEBs latitudes using Method 2. The median of these is plotted against minimum Dst for each of the simulations in the bottom panel of Figure 8 as red diamonds. In addition, the $25\% - 75\%$ confidence intervals are plotted as red errorbars, and the total range of calculated boundaries values are plotted as green errorbars. The median boundary values calculated using Method 2 appear to match the historical boundaries calculated for days with Dst > -600 nT, with the auroral latitude moving mostly linearly South with decreasing Dst to this point. A simple fit was applied to the median calculated auroral boundary locations (shown as a black line). This takes the form

$$\text{Boundary (MLAT)} = 33.8 - \frac{16,770}{\text{Dst} - 584}, \qquad (-1150 < \text{Dst} < 0 \text{ nT}) \tag{7}$$

The shaded black region shows a fit of the same form applied to the 25% and 75% confidence intervals. Equation 6 returns slightly lower calculated MEAEB values than Equation 7.

While the median MEAEB latitude values for all of the simulations are above 40°, the three largest storm simulations (with Dst < -1000 nT) saw calculated boundaries at certain longitudes dip below 40° N. The lowest calculated boundary was 35.5° for the simulation with a minimum Dst of -1054 nT. This low-latitude boundary value can be compared to the historical Carrington event, albeit indirectly. While there are not enough existing surface magnetic field data from the Carrington event to directly calculate the MEAEB as above, the location of the auroral latitude for this event can be inferred. One existing surface magnetic field dataset for the Carrington event is from Rome. This dataset saw an extremely large horizontal magnetic field deviation, which, when coupled with very low-latitude auroral sightings, indicate that the auroral oval was at least as far South as Rome (38.6° magnetic N) in 1859 [*Blake et al.*, 2020; *Hayakawa et al.*, 2019]. This indicates that the MEAEB estimates for our largest simulations are consistent with actual superstorm values.

5. Comparing Algorithm Outputs to other Auroral Phenomena

As can be seen in Figures 7 and 9, the algorithm outlined in this paper can separate the geomagnetically active poleward regions from the more geomagnetically quiet equatorward regions. Throughout the paper, we have labelled these calculated points as the maximum extents of the auroral equatorward boundaries (or MEAEBs). In this section, we compare the algorithm output values to auroral equatorward boundaries estimated using precipitating electron data taken by satellite, as well as the location of the polar cap boundary for two of the SWMF simulations.

5.1. Comparison with Empirical Auroral Model

On successive orbits from its launch in 2003, the Defense Meteorological Satellite Program (DMSP) f16 satellite measured the mean energy and energy flux of precipitating electrons in the auroral oval with extreme ultraviolet to far ultraviolet images taken using the Special Sensor Ultraviolet Spectrographic Imager (SSUSI) instrument. By identifying areas with energy flux thresholds above 0.2 $\mathrm{ergs\,s^{-1}cm^{-2}}$, an initial nightside auroral boundary is identified. This boundary is then combined with a pre-calculated auroral boundary using the Global UltraViolet Imager (aboard the TIMED satellite, see *Zhang & Paxton* [2008]) data to get an equatorward boundary estimate for an orbit. These data, along with other along with other products such as identification of discrete auroral arcs, can be found at https://ssusi.jhuapl.edu/, along with a detailed description of the algorithms used. The SSUSI-derived auroral boundary model data are available from 2005 to 2016. In this time-period, the minimum Dst was -247 nT. For 855 randomly selected days in this time-period (including the 100 most disturbed days by Dst), the most equatorward location of the boundaries derived by the SSUSI-derived auroral boundary model were recorded, and compared to our calculated MEAEBs for the same days. This is shown in Figure 10.

In comparison to the SSUSI based model, our algorithm predicts more poleward MEAEBs as the minimum Dst of the day decreases (with slope = 1.35). In addition, there are many geomagnetically quiet days (Dst > -15) for which the SSUSI model gives a very low minimum latitude value ($< 52°$). A least absolute difference linear fit (which effectively weighs these outliers less) is shown in Figure 10. The outputs from our algorithm, which estimates the location of the auroral boundary using surface geomagnetic data (a proxy for electric currents in the ionosphere) gives similar estimates to the electron-precipitation based model. That the two empirical models are not perfectly correlated is unsurprising, as they in effect measure different phenomena associated with the auroral boundary, in order to estimate its daily most equatorward position. Different caveats also exist for each method. In the case of the SSUSI-derived boundaries, that model was made with a limited number of available large-scale (high Kp) geomagnetic events. In addition, the look angle of the instrument can affect measurements (see https://ssusi.jhuapl.edu/data_algorithms for more).

In addition to the SSUSI model, There are also other auroral boundary models that rely on electron precipitation and satellite data, and have been calculated for different time-periods. These include *Zhang & Paxton* [2008]; *Kilcommons et al.* [2017]; *Carbary* [2005] and *Ding et al.* [2017] for example. *Sigernes et al.* [2011] compares ground-based and satellite based estimates for the auroral oval. Further research could combine our MEAEB algorithm with precipitation data to estimate the auroral oval boundaries.

5.2. Comparison to Simulated Polar Cap Boundaries

Next, we compare our calculated MEAEBs (using both Method 1 and 2) with the polar cap boundary for two of the SWMF simulations (20-11-2003 and Scaled-B6 in Table 1. The polar cap boundary, which will be a few degrees North of the auroral equatorward boundary (depending on the width of the auroral oval), separates the closed and open geomagnetic field lines. With significant solar wind forcing and reconnection, the polar cap expands, but also shifts towards the dayside [*Ngwira et al.*, 2014]. This brings the ionospheric current systems to lower latitudes, and with them an increase in surface magnetic field variations. Figure 11 shows the unscaled 20-21 November 2003 and Scaled-B4 simulations at snapshots when the respective simulations saw the largest expansion of the polar cap boundary. The top row shows total current density in the near-Earth magnetosphere, and the bottom row shows the normalized electric field in the Northern hemisphere, with the 2D extent of the polar cap boundary.

The scaled simulation shows a more compressed magnetopause when compared to the unscaled simulation. This corresponds to a lower dayside polar cap (at 34.5°N MLAT) when compared to the unscaled simulation (41.5° N MLAT). Figure 12 shows how the calculated auroral boundaries compare to the most equatorward extent of the polar cap boundaries for both of the simulations. In both of these instances, the auroral boundaries calculated using Method 1 (interpolated INTERMAGNET sites) were less than 3° further South than the most equatorward position of the polar cap boundary. The boundaries calculated using Method 2 (i.e., all SWMF simulated geomagnetic field data) intersects with the minimum latitude polar cap boundary in places. In reality, the location of the polar cap boundary and auroral oval should be close, but are not necessarily coincident, with the polarcap boundary expected to be North of the auroral oval (and its emissions) by a few degrees [*Carbary*, 2005]. Figure 12 shows that the boundary calculated using only SWMF simulated geomagnetic data is closely related to the extent of the polar cap boundary.

6. Discussion and Conclusion

In this paper, we have outlined a simple algorithm to estimate the maximum extent of the auroral equatorward boundary from simulated and historical surface geomagnetic field data. This method was applied to horizontal geomagnetic field data from INTERMAGNET stations from 1991-2016, as well as data for the March 1989 storm. The calculated auroral equatorward boundaries were shown to be further South as a day's minimum Dst decreased. For $-400 < \mathrm{Dst} < 0$ nT, there appears to be a scatter of $\sim 8°$ MLAT where the maximum extent of the auroral boundary is located. The lack of extreme geomagnetic storm days in the database means it is hard to estimate the range of MEAEBs for Dst< -400 nT, although the boundaries can be seen to continue equatorward for what data exist. The most disturbed day for which we have widespread geomagnetic data is the

14 March 1989, with a minimum Dst= -589 nT. This had a calculated auroral boundary of $45° \pm 3.8°$ MLAT.

A number of geomagnetic storms of different intensities (ranging from minimum Dst values of -1 nT to -1142 nT) were then simulated using a high resolution setup of the Space Weather Modeling Framework. From the geomagnetic field outputs of these simulations, the MEAEBs were calculated using 1) interpolated geomagnetic field values at INTERMAGNET locations and 2) using all simulated geomagnetic data to get a 2D estimate of the extent of the auroral oval. For both of these methods, the calculated MEAEBs for the simulations broadly match with the calculated MEAEBs for historical geomagnetic data (i.e., for Dst > -600 nT). This indicates that for low to medium-intensity geomagnetic storms, the SWMF setup used here can replicate the geomagnetic signal of the auroral oval.

For Dst values between 0 to around -600 nT, the extent of the simulated auroral boundaries appears to move equatorward mostly linearly (from $> 60°$ to $\sim 44°$). A massive increase in the intensity of the simulated storms (from Dst -600 to < -1000 nT) resulted in an only slightly more equatorward auroral boundary (down to $\sim 40°$). The most extreme simulated storms (Dst < -1000 nT) had calculated MEAEBs as far South as 35.5° N in places (as calculated using Method 2), and a large scatter. There are not enough worldwide magnetic field data available to directly apply our auroral boundary algorithm to any historical storm day of similar intensity (in terms of Dst). That said, the low latitude auroral boundaries in our large storms ($< 40°$ N) are consistent with the estimated auroral oval location of the Carrington event (at least 38.6° N) [*Blake et al.*, 2020].

Our MEAEB estimates were compared to an empirical auroral boundary model using satellite electron precipitation data for a 855 days between 2005 and 2016. Our boundary estimates are broadly in line with the SSUSI-derived model, although it should be noted that our algorithm in effect uses the magnetic signature of electrical currents in the ionosphere, as opposed to electron precipitation. Future work should more comprehensively compare our estimates to the various empirical satellite based auroral boundary models for a larger time-period. In addition to this, the MAEABs for two simulations were found to be closely related to the maximum equatorward extent of the polar cap boundary, as expected.

The relationship between the size of a geomagnetic disturbance and the location of the auroral oval is particularly important when estimating the effects of extreme events. A common approach to estimating peak geomagnetic and geoelectric field values for an extreme geomagnetic superstorm for a location is to apply different fits to distributions of all available historical measurements [*Pulkkinen et al.*, 2008, 2012; *Thomson et al.*, 2011; *Love et al.*, 2016; *Love*, 2020; *Riley & Love*, 2017]. As digital magnetic field data is typically available for only a few decades (depending on the location), a low or mid-latitude location may have been only subauroral for all available data. Depending on the location, such a site may become engulfed by magnetic variations from the auroral oval as it expands during an extreme storm. Extrapolating from measured geomagnetic field data for an extreme geomagnetic storm estimate may therefore underestimate peak geomagnetic field values in this scenario.

The large scatter in calculated auroral oval latitude for the more extreme simulations may be indicative of a suboptimal simulation setup, and different parameters may be needed to adequately simulate extreme geomagnetic storms. For example, the radial component of the total magnetic field can be forced to coincide with the B0 field in future simulations. It may be useful to re-run the larger simulations using greater resolution in the different SWMF models used. In addition, the combination of BATS-R-US, RCM and RIM is just one possible configuration that can be used to simulate geomagnetic storms, and the position of the auroral boundary will be explored in the future with different SWMF models. An example of this is the comprehensive inner magnetosphere-ionosphere model (CIMI) [*Fok et al.*, 2014]. In addition, all of the storms here represent a limited number of solar wind templates. In particular, all of the storms that resulted in a Dst< -1000 nT were scaled versions of the 20-21 November 2003 storm event. CMEs with different orientations and substructures will have varying levels of geo-effectiveness. Future studies will use more varied large-scale solar wind inputs. In particular, efforts are being undertaken to simulate a storm which will more accurately replicate aspects of the Carrington event (i.e., the quick recovery in the geomagnetic field at low-latitudes).

Appendix A: Location of Inner Magnetospheric Current Mapping in SWMF Simulations

The latitude at which a magnetic field line at an L-shell L touches the surface of the Earth can be described by

$$\Lambda = \arccos\sqrt{\frac{1}{L}} \tag{A1}$$

For smaller L values, the magnetic field line will have a footprint at a lower latitude. As outlined in Section 3, the location of the inner boundary of the magnetospheric domain (R_{body}) and the location at which the magnetospheric currents are mapped (R_{curr}) are two parameters that can be altered when running the BATS-R-US simulation. The values chosen can have a marked effect on the distribution of B_H at the Earth's surface.

Through the course of running the simulations in this paper, it was found that for more intense solar wind drivers, these values needed to be lowered, in order to avoid sharp discontinuities in the surface geomagnetic field. As the R_{body} parameter is increased, the footprint of the FACs which connect the magnetosphere to ionosphere is mapped to higher latitudes. This is highlighted in Figure 13, which shows the maximum SWMF-calculated B_H at every point on the Earth's surface for three test simulations. Each of these simulations used the SWPC v2 high resolution BATS-R-US grid (approximately 1.9 million cells, minimum cell size = $1/8\,R_E$), and were driven using the 'Scaled-B4' solar wind conditions (see Table 1). Different values for R_{body} and R_{curr} were used for each of these runs, and the corresponding Λ latitudes are plotted as horizontal dashed white lines (SWPC's operational run uses $R_{body} = 2.5\,R_E$ and $R_{curr} = 3.0\,R_E$).

For the runs with $R_{curr} = 3.5\,R_E$ and $R_{curr} = 3.0\,R_E$, there is a sharp discontinuity in ΔB_H at the Λ-latitudes in both hemispheres. For the run with $R_{curr} = 1.8\,R_E$, there are clearly auroral and subauroral regions, but this is not demarcated by the Λ-latitudes.

For each of the 15 simulations shown in Table 1, a suitably small R_{curr} value was chosen such that no sharp discontinuity in ΔB_H was seen. We recommend that R_{curr} is set to a value less than 3 R_{curr} when an intense geomagnetic disturbance is to be simulated.

Acknowledgments.

Calculated MEAEBs for historical days and SWMF simulations are given as supporting information, along with the maximum calculated E_H values for each of the simulations. These data, along with example Python scripts used to calculate the MEAEBs can be found at https://doi.org/10.5281/zenodo.4035207. The results presented in this paper rely on data collected at magnetic observatories. We thank the national institutes that support them and INTERMAGNET for promoting high standards of magnetic observatory practice (www.intermagnet.org). Data were also obtained from the SuperMAG database (http://supermag.jhuapl.edu/info/?page=faq). Dst values were obtained from the World Data Center for Geomagnetism, Kyoto (http://wdc.kugi.kyoto-u.ac.jp/). Solar wind data were accessed using the NASA OMNIweb dataportal (omniweb.gsfc.nasa.gov). SWMF simulations were performed on the NASA Center for Climate Simulation's Discover cluster. SSUSI-derived model auroral boundary data were taken from https://ssusi.jhuapl.edu/. This work was supported by the NASA's Living With a Star program (17-LWS17_2-0042), and the Electric Power Research Institute (EPRI SAA5-2017-4-R26568). Gábor Tóth was supported by the NSF PRE-EVENTS grant 1663800. We extend our thanks to Steve Morley, Bob Aritt, Jenn Gannon and Larry Paxton for their valuable discussion. We thank both of the reviewers for their useful comments and feedback during the review process.

References

Allen, J., Frank, L., Sauer, H., Reiff, P., (1989) Effects of the March 1989 Solar Activity, *EOS*, *70 46* https://doi.org/XXXXXXXX

Blake, S.P., Pulkkinen, A., Schuck, P.W., Nevanlinna, H., Reale, O., Veenadhari, B., Mukherjee, S., (2020) Magnetic Field Measurements from Rome during the August-September 1859 Storms, *J. Geophys. Res.*, *XX XXXX* https://doi.org/10.1029/2019JA027336

Bolduc, L., (2002) GIC observations and studies in the Hydro-Quebec power system, *J. Atmos. Sol.-Terr. Phys.*, *64 1793–1802* https://doi.org/10.1016/S1364-6826(02)00128-1

Boteler, D.H, Pirjola, R.J., (1998) The complex-image method for calculating the magnetic and electric fields produced at the surface of the Earth by the auroral electrojet, *Geophys. J. Int.*, *132 31-40* https://doi.org/10.1046/j.1365-246x.1998.00388.x

Buonsanto, M., (1999) Ionospheric Storms - A Review, *Space Science Reviews*, *88 563-601* https://doi.org/10.1023/A:1005107532631

Carbary, J.F., Sotirelis, T., Newell, P.T., Meng, C.I., (2003) Auroral boundary correlations between UVI and DMSP, *J. Geophys. Res.*, *108 A1* https://doi:10.1029/2002JA009378

Carbary, J.F., (2005) A Kp-based model of auroral boundaries, *Space Weather*, *3 S10001* https://doi:10.1029/2005SW000162

Cliver, E.W, Dietrich, W.F, (2013) The 1859 space weather event revisited: limits of extreme activity, *J. Space Weather Space Clim.*, *3 A31* https://doi.org/10.1051/swsc/2013053

Dinge, G.X., He, F., Zhang, X.X., Chen, B., (2017) A new auroral boundary determination algorithm based on observations from TIMED/GUVI and DMSP/SSUSI, *J. Geophys. Res.*, *122 2162-2173* https://doi.org/10.1002/2016JA023295

De Zeeuw, D.L., Gombosi, T.I., Groth, C.P.T., Powell, K.G., Stout, Q.F., (2000) An Adaptive MHD Method for Global Space Weather Simulations, *IEEE Trans. on Plasma Science*, *28 6* https://doi.org/10.1109/27.902224

De Zeeuw, D.L., Sazykin, S., Wolf, R.A., Gombosi, T.I., Ridley, A.J., Toth, G., (2004) Coupling of a global MHD code and an inner magnetospheric model: Initial results, *Journal of Geophysical Research*, *109 A12219* https://doi.org/10.1029/2003JA010366

Eroshenko, E.A., Belov, A.V., Boteler, D., Gaidash, S.P., Lobkov, S.L., Pirjola, R., Trichtchenko, L., (2010) Effects of strong geomagnetic storms on Northern railways in Russia, *Adv. Space Res.*, *46 1102-1110* https://doi.org/10.1016/j.asr.2010.05.017

Fok, M.C., Buzulukova, N.Y., Chen, S.H., Glocer, A., Nagai, T., Valek, P., Perez, J.D., (2014) The Comprehensive Inner Magnetosphere-Ionosphere Model, *J. Geophys. Res. Space Physics*, *119 7522-7540* https://doi.org/10.1002/2014JA020239

Gonzalez, W.D., Clúa de Gonzalez, A.L., Dal Lago, A., Tsurutani, B.T., Arballo, J.K., Lakhina, G.K., Buti, B., Ho, C.M, Wu, S.-T.(1998) Magnetic cloud field intensities and solar wind velocities, *Geophysical Research Letters*, *25 963-966* https://doi.org/10.1029/98GL00703

Haiducek, J.D., Welling, D.T., Ganushkina, N.Y., Morley, S.K., Ozturk, D.S., (2017), SWMF global magnetosphere simulations of January 2005: Geomagnetic indices and cross-polar cap potential, *Space Weather*, *15 1567-1587* https://doi.org/10.1002/2017SW001695

Hayakawa, H., Iwahashi, K., Tamazawa, H., Isobe, H., Kataoka, R., Ebihara, Y., Miyahara, Kawamura, A.D., Shibata, K., (2016), East Asian observations of low-latitude aurora during the Carrington magnetic storm *Pub. Astron. Soc. Japan*, *68 99* https://doi.org/10.1093/pasj/psw097

Hayakawa, H., Ebihara, Y., Hand, D.P., Hayakawa, S., Kumar, S., Mukherjee, S., Veenadhari, B., (2018), Low-latitude Aurorae during the Extreme Space Weather Events in 1859, *The Astrophysical Journal*, *869:57* https://doi:10.3847/1538-4357/aae47c

Hayakawa, H., Ebihara, Y., Willis, D.M., et al., (2019), Temporal and Spatial Evolutions of a Large Sunspot Group and Great Auroral Storms around the Carrington Event in 1859, *Space Weather*, *869:57* https://doi:10.1029/2019SW002269

Kilcommons, L.M., Redmon, R.J., Knipp, D.J., (2017) A new DMSP magnetometer and auroral boundary data set and estimates of field-aligned currents in dynamic auroral boundary coordinates, *J. Geophys. Res. Space Physics*, *122 9068-9079* https://doi.org/10.1002/2016JA023342

Li, X., Temerin, M., Tsurutani, B.T., Alex, S., (2006) Modeling of 1-2 September 1859 super magnetic storm, *Adv. Space Res.*, *38 273–279* https://doi.org/10.1016/j.asr.2005.06.070

Love, J.J., Gannon, J.L., (2009) Revised Dst and the epicycles of magnetic disturbance: 1958-2007, *Ann. Geophys*, *27 3101-3131* https://doi.org/10.5194/angeo-27-3101-2009

Love, J.L., Coisson, P., Pulkkinen, A., (2016), Global statistical maps of extreme-event magnetic observatory 1 min first differences in horizontal intensity, *Geophy. Res. Letters*, *43 4126-4135* https://doi:10.1002/2016GL068664

Love, J.L., Hayakawa, H., Cliver, E.W., (2019), Intensity and Impact of the New York Railroad Superstorm of May 1921, *Space Weather*, *17* https://doi:10.1029/2019SW002250

Love, J.L., (2020), Some Experiments in Extreme-Value Statistical Modeling of Magnetic Superstorm Intensities, *Space Weather*, *18 4126-4135* https://doi:10.1029/2019SW002255

Manchester IV, W.B., Ridley, A.J., Gombosi, T.I., DeZeeuw, D.L., (2005), Modeling the Sun-to-Earth propagation of a very fast CME, *Advances in Space Research*, *38* https://doi.org/10.1016/j.asr.2005.09.044

Milan, S.E., Hutchinson, J., Boakes, P.D., Hubert, B., (2009), Influences on the radius of the auroral oval, *Ann. Geophys.*, *27 2913-2924* https://doi.org/10.5194/angeo-27-2913-2009

Ngwira, C.M., Pulkkinen, A., Mays, M.L., Kuznetsova, M.M., Galvin, A.B., Simunac, K., Baker, D.N., Li, X., Zheng, Y., Glocer, A., (2013), Simulation of the 23 July 2012 extreme space weather event: What if this extremely rare CME was Earth directed, *Space Weather*, *11 671-679* https://doi:10.1002/2013SW000990

Ngwira, C.M., Pulkkinen, A., Wilder, F.D., Crowley, G., (2013), Extended study of extreme geoelectric field event scenarios for geomagnetically induced current applications, *Space Weather*, *11 121-131* https://doi:10.1002/swe.20021

Ngwira, C.M., Pulkkinen, Kuznetsova, M.M., Glocer, A., (2014), Modeling extreme "Carrington-type" space weather events using three-dimensional global MHD simulations, *J. Geophys. Res. Space Physics*, *119 4456-4474* https://doi:10.1002/2013JA019661

Powell, K.G., Roe, P.L., Linde, T.J., Gombosi, T.I., De Zeeuw, D.L., (1999), A Solution-Adaptive Upwind Scheme for Ideal Magnetohydrodynamics, *Journal of Computational Physics*, *154 284-309* https://doi.org/10.1006/jcph.1999.6299

Pirjola, R., Viljanen, A., Pulkkinen, A., Amm, O., (1999), Space Weather Risk in Power Systems and Pipelines, *Phys. Chem. Earth*, *25 333-337* https://doi.org/10.1016/S1464-1917(00)00027-1

Pirjola, R., (2001), Review on the calculation of surface electric and magnetic fields and of geomagnetically induced currents in ground-based technological systems, *Surveys in*

Geophysics, *23 71-90* https://doi.org/10.1023/A:1014816009303

Pulkkinen, A., Pirjola, R., Viljanen, A., (2008), Statistics of extreme geomagnetically induced current events, *Space Weather*, *6 S07001* https://doi.org/10.1029/2008SW000388

Pulkkinen, A., Bernabeu, E., Eichner, J., Beggan, C., Thomson, A.W.P., (2012), Generation of 100-year geomagnetically induced currents, *Space Weather*, *10 S04003* https://doi.org/10.1029/2011SW000750

Pulkkinen, A., Rastatter, L., Kuznetsova, M., Singer, H., Balch, C., Weimer, D., Toth, G., Ridley, A., Gombosi, T., Wiltberger, M., Raeder, J., Weigel, R., (2013), Community-wide validation of geospace model ground magnetic field perturbation predictions to support model transition to operations, *Space Weather*, *11 369-385* https://doi.org/10.1002/swe.20056

Pulkkinen, A., Bernabeu, E., Eichner, J., Viljanen, A., Ngwira, C., (2015), Regional-scale high-latitude extreme geoelectric fields pertaining to geomagnetically induced currents, *Earth, Planets and Space*, *67 93* https://doi.org/10.1186/s40623-015-0255-6

Pulkkinen, A., et al. (2017), Geomagnetically induced currents: Science, engineering and applications readiness, *Space Weather*, *15 826-856* https://doi:10.1002/2016SW001501

Ridley, A.J., Gombosi, T.I., DeZeeuw, D.L. (2004), Ionospheric control of the magnetosphere: conductance, *Ann. Geophys*, *22 567-584* https://doi:10.5194/angeo-22-567-2004

Riley, P., Love, J.J. (2017), Extreme geomagnetic storms: Probabilistic forecasts and their uncertainties, *Space Weather*, *15 53-64* https://doi.org/10.1002/2016SW001470

Russell, C.T., Luhmann, J.G., Strangeway, R.J., (2016), Space Physics: An Introduction, *Cambridge University Press*, ISBN:978-1-107-09882-4

Shepherd, S.G., (2014), Altitude-Adjusted Corrected Geomagnetic Coordinates: Definition and Functional Approximations, *J. Geophys. Res.*, *119* https://doi.org/10.1002/2014JA020264

Shea, M.A., Smart, D.F., (2006), Compendium of the eight articles on the "Carrington Event" attributed to or written by Elias Loomis in the American Journal of Science, 1859-1861, *Adv. in Space Research*, *38 313-385* https://doi:10.2475/ajs.s2-32.96.318

Sigernes, F., et al. (2011), Two methods to forecast auroral displays, *J. Space Weather Space Clim.*, *1 A03* https://doi.org/10.1051/swsc/2011003

Silverman, S.M., Cliver, E.W., (2001), Low-latitude auroras: the magnetic storm of 14-15 May 1921, *J. Atmos. Sol.-Terr. Phys.*, *63 523-535* https://doi.org/10.1016/S1364-6826(00)00174-7

Silverman, S.M., (2003), Sporadic auroras, *J. Geophys. Res.*, *108(A4)* https://doi.org/10.1029/2002JA009335

Silverman, S.M., (2005) Comparison of the aurora of September 1/2, 1859 with other great auroras, *Adv. in Space Res.*, *38 136–144* https://doi.org/10.1016/j.asr.2005.03.157

Stephenson, F., Willis, D., Hallinan, T. (2004), The earliest datable observation of the aurora borealis, *Astronomy & Geophysics*, *45 615–617* https://doi.org/10.1046/j.1468-4004.2003.45615.x

Stern, D.P., (2002), A Millenium of Magnetism, *Reviews of Geophysics*, *40 3* https://doi:10.1029/2000RG000097

Thomson, A.W.P., Dawson, E.B., Reay, S.J., (2011) Quantifying extreme behavior in geomagnetic activity, *Space Weather*, *9 S10001* https://doi:10.1029/2011SW000696

Tóth, G. et al., (2005) Space Weather Modeling Framework: A new tool for the space science community, *J. Geophys. Res.*, *110 A12226* https://doi:10.1029/2005JA011126

Tóth, G. et al., (2012) Adaptive numerical algorithms in space weather modeling, *Journal of Computational Physics*, *231* https://doi:10.1016/j.jcp.2011.02.006

Tóth, G., Meng, X, Gombosi, T.I., Rastätter, L., (2014) Predicting the Time Derivative of Local Magnetic Perturbations, *Journal of Geophys. Res.*, *119 310* https://doi:10.1002/2013JA019456

Toffoletto, F., Sazykin, S., Spiro, R., Wolf, R., (2003) Inner Magnetospheric Modeling with the Rice Convection Model, *Space Science Reviews*, *107 175-196* https://doi.org/10.1023/A:1025532008047

Tsurutani, B.T., Gonzalez, W.D., Lakhina, G.S., Alex, S., (2003) The extreme magnetic storm of 1-2 September 1859, *J. Geophys. Res.*, *108 A7* https://doi:10.1029/2002JA009504

Wanliss, J., Showalter, K.M., (2006) High-resolution global storm index: Dst versus SYM-H, *J. Geophys. Res.*, *111 A02202* https://doi:10.1029/2005JA011034

Woltring, H.J., (1986) A Fortran package for generalized, cross-validatory spline smoothing and differentiation, *Adv. Eng. Software*, *8 104-113* https://doi.org/10.1016/0141-1195(86)90098-7

Woodroffe, J.R., Morley, S.K., Jordanova, V.K., Henderson, M.G., Cowee, M.M., Gjerloev, J.G., (2016) The latitudinal variation of geoelectromagnetic disturbances during large (Dst ≤ -100 nT) geomagnetic storms, *Space Weather*, *14 668-681* https://doi:10.1002/2016SW001376

Yokoyama, N., Kamide, Y., Miyaoka, H. (1997) The size of the auroral belt during magnetic storms, *Ann. Geophys.*, *16 566-573* https://doi.org/10.1007/s00585-998-0566-z

Welling, D., Love, J.J., Rigler, E.J., Oliveira, D.M., Komar, C.M.(2020), Numerical simulations of the geospace response to the arrival of a perfect interplanetary coronal mass ejection, *submitted to Geophys. Res. Letters*, https://doi.org/10.1002/essoar.10502106.1

Zhang, Y., Paxton, L.J., (2008), An empirical Kp-dependent global auroral model based on TIMED/GUVI FUV data, *Journal of Atmospheric and Solar-Terrestrial Physics*, *70 1231-1242* https://doi.org/10.1016/j.jastp.2008.03.008

/home/blake/Drive/NASA_Data/Paper_Lat_Thresh/Submission/First_corrections/IMAGES

Figure 1. Top: Measured horizontal magnetic field values (after a baseline is removed) at Eskdalemuir during the Halloween storms of 2003. Bottom: calculated horizontal electric field using the resistive Quebec model and Equations 2,3. Eskdalemuir had a magnetic latitude = 57.8°N for this storm, and a maximum calculated $E_H = 2$ Vkm^{-1}.

/home/blake/Drive/NASA_Data/Paper_Lat_Thresh/Submission/First_corrections/IMAG

Figure 2. Maximum calculated E_H vs. magnetic latitude for 30 October 2003. The maximum electric field values can be clearly seen to increase sharply around $\pm 50°$ when moving poleward. This marks the MEAEB zone for the duration of the storm.

/home/blake/Drive/NASA_Data/Paper_Lat_Thresh/Submission/First_corrections/IMAGES

Figure 3. Maximum calculated E_H vs. magnetic latitude for two different days. The blue and red dots are for INTERMAGNET sites for a stormy (30 Oct. 2003, Dst = -383 nT) and quiet (07 Oct 2009, Dst = 0 nT) days respectively. Bold lines are for the smoothed spline fits. Dashed vertical lines mark the points where the gradients for the fit lines are the greatest. These mark the calculated auroral boundaries (MEAEBs) for the two days.

/home/blake/Drive/NASA_Data/Paper_Lat_Thresh/Submission/First_corrections/IMAG

Figure 4. Daily calculated MEAEB against daily minimum Dst values from INTERMAGNET data (1991-2016). In addition, the 12-14 March 1989 days were included using SuperMag data. Errorbars are 1σ estimates from 500 bootstrapped sample fits.

/home/blake/Drive/NASA_Data/Paper_Lat_Thresh/Submission/First_corrections/IMAGES

Figure 5. MEAEB calculations when the number of magnetic observatories used varies. The left panel is for 30 October 2003, and the right panel is for 17 March 2015. The 90% confidence intervals can be seen to narrow as the number of observatories increases.

/home/blake/Drive/NASA_Data/Paper_Lat_Thresh/Submission/First_corrections/IMAG

Figure 6. Solar wind conditions for 20-21 November 2003 storm. These data were taken from the NASA OMNIWeb portal (https://omniweb.gsfc.nasa.gov/), and were scaled to simulate more intense storms. Red vertical dashed line indicates the time after which the time-series were scaled.

Date From	**Min. B_Z**	**Min. V_X**	**Max. n**	**Real Dst**	**SWMF Dst**
DD-MM-YYYY	nT	kms^{-1}	cm^{-3}	nT	nT
23-07-2014	-5.21	-388	18.5	0	-1
29-05-2010	-13.84	-523	25.8	-80	-7
14-12-2006	-17.41	-916	16.7	-162	-46.5
21-10-2001	-28.85	-705	65.28	-187	-202
15-05-2005	-48.26	-984	33.1	-247	-284
08-11-2004 (A)	-48.53	-722	55.36	-374	-263
20-11-2003 (B)	-52.33	-751	28.7	-422	-383
Scaled-A1	-70.5	-1426	80	-	-485
Scaled-B1	-60.18	-1051	42.9	-	-497
Scaled-B2	-68.03	-1351	57.3	-	-681
Scaled-A2	-94	-1902	110	-	-757
Scaled-B3	-75.88	-1652	85.9	-	-916
Scaled-B4	-78.5	-1749	95.4	-	-1053
Scaled-B5	-81.1	-1847	105.2	-	-1059
Scaled-B6	-83.73	-1945	114.6	-	-1142

Table 1. Selected maxima and minima for the simulated events. The B_Z, V_X, and n columns refer to the solar wind inputs used for the simulations. The 'Real Dst' column is the minimum Dst for the real events. The 'SWMF Dst' column is the minimum calculated Dst from the output of the simulations. The scaled events used scaled solar wind inputs from two historical periods (A and B).

/home/blake/Drive/NASA_Data/Paper_Lat_Thresh/Submission/First_corrections/IMAGES/7_ME

Figure 7. The normalized calculated E_H values for the Northern hemisphere for 12 of the SWMF simulations. White dots show the locations of the INTERMAGNET sites at which the simulated geomagnetic field was interpolated. Red horizontal lines show the calculated locations of the MEAEB, and yellow lines show the bootstrapped 1σ errorbars.

/home/blake/Drive/NASA_Data/Paper_Lat_Thresh/Submission/First_corrections/IMAGES/8_D

Figure 8. Minimum Dst versus calculated MEAEB latitudes for INTERMAGNET data and SWMF simulation outputs. Top: SWMF MEAEBs calculated using interpolated INTERMAGNET sites (Method 1, red stars). Errorbars are 1σ estimates from bootstrapped spline fits. Bottom: SWMF MEAEBs calculated using all surface magnetic field data (Method 2, red diamonds). The 25%-75% confidence intervals are shown as red errorbars and the total range of calculated boundaries are shown as green errorbars. For both panels, the shaded black lines show simple fits applied to the data (Equations 6 and 7).

/home/blake/Drive/NASA_Data/Paper_Lat_Thresh/Submission/First_corrections/IMAGES/9_ME

Figure 9. The normalized calculated E_H values for the Northern hemisphere for 12 of the SWMF simulations. The bold red lines mark the location of the MEAEB calculated using all of the output surface magnetic field data (Method 2 outlined in the text).

/home/blake/Drive/NASA_Data/Paper_Lat_Thresh/Submission/Second_corrections/IMAGES/10_

Figure 10. Comparison between calculated equatorward auroral boundaries using our algorithm (x-axis) and the SSUSI-derived empirical model (y-axis). Dashed black line shows the 1:1 reference line., and red dashed line is a least absolute difference linear fit.

/home/blake/Drive/NASA_Data/Paper_Lat_Thresh/Submission/First_corrections/IMAGES/11

Figure 11. Comparison between the unscaled November 2003 simulation (left column) and scaled simulation (right column). The top row shows the total current density in near-Earth magnetosphere. Black and white lines show open and closed field lines respectively. Red lines are the highest latitude closed field lines. The bottom row shows a snapshot of the normalized electric field in the Northern hemisphere, with the 2D position of the polar cap boundary.

/home/blake/Drive/NASA_Data/Paper_Lat_Thresh/Submission/First_corrections/IMAGES/12_F

Figure 12. Calculated MEAEB using the geomagnetic field data and Method 1 & 2 outlined in Section 4 (red and blue lines, respectively), and the minimum latitude of the polar cap boundary (green line) for the two comparison simulations.

/home/blake/Drive/NASA_Data/Paper_Lat_Thresh/Submission/First_corrections/IMAGES/13_R

Figure 13. Maximum B_H on Earth for three test simulations using the SWPC grid. All three simulations were run using the Scaled-B4 solar wind inputs (see Table 1), but had different R_{body} and R_{curr} parameter values. The dashed white lines correspond to Λ values calculated from Equation A1 using the R_{curr} for each simulation.

Figure 1.

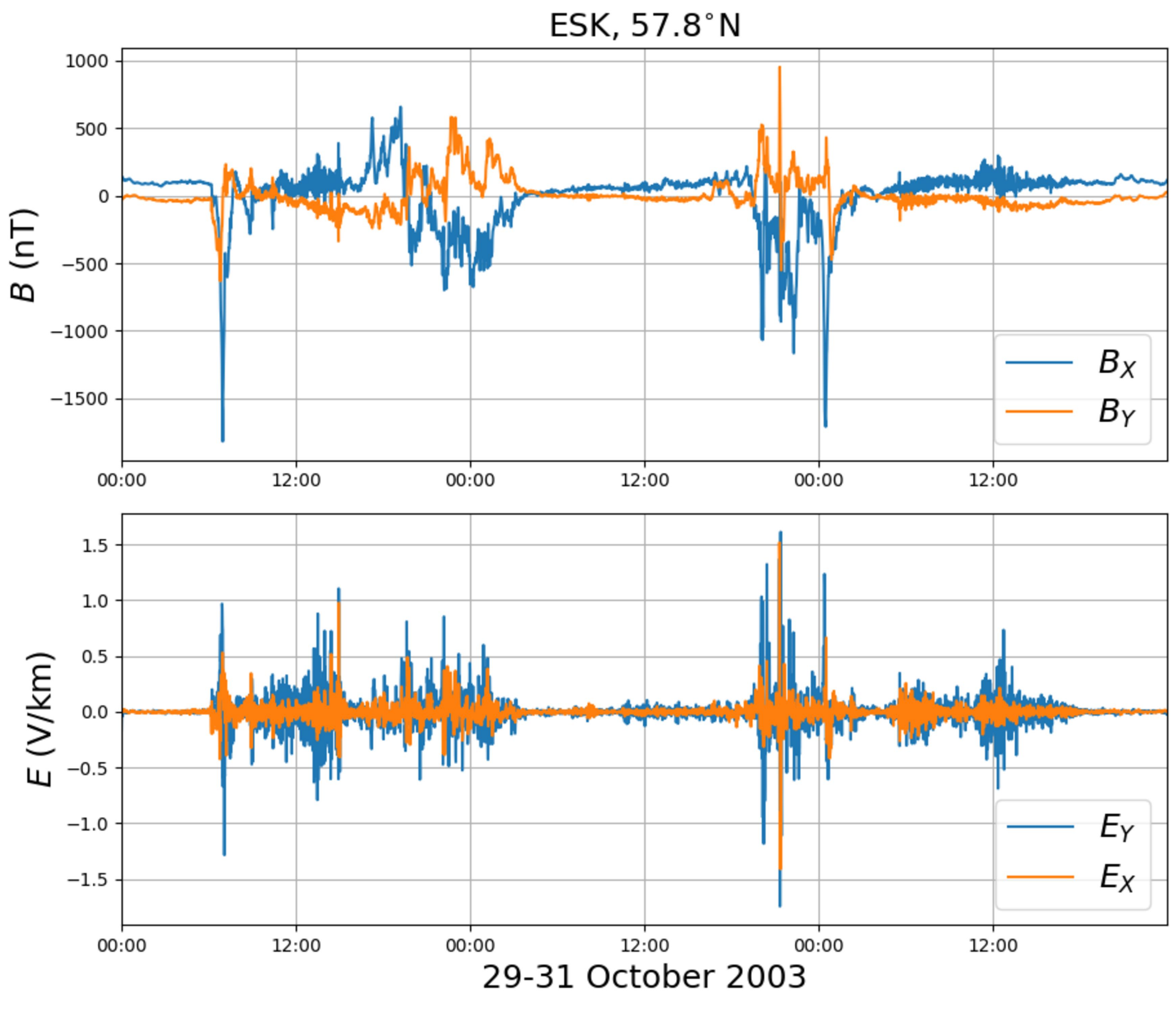
ESK, 57.8°N
B (nT)
1000
500
0
−500
−1000
−1500
B_X
B_Y
00:00
12:00
00:00
12:00
00:00
12:00
E (V/km)
1.5
1.0
0.5
0.0
−0.5
−1.0
−1.5
E_Y
E_X
00:00
12:00
00:00
12:00
00:00
12:00
29-31 October 2003

Figure 2.

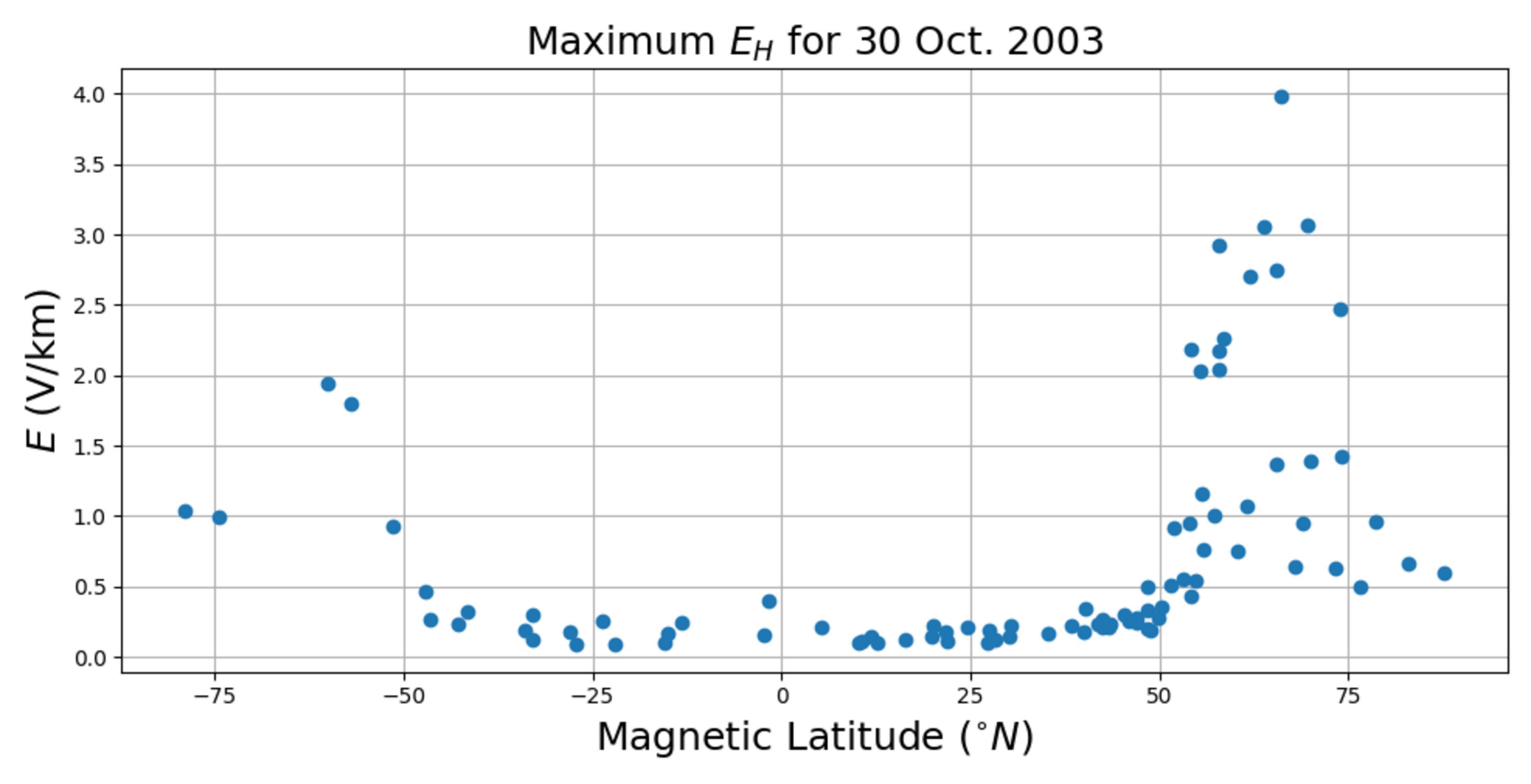
Maximum E_H for 30 Oct. 2003
E (V/km)
Magnetic Latitude ($^\circ N$)
4.0
3.5
3.0
2.5
2.0
1.5
1.0
0.5
0.0
−75
−50
−25
0
25
50
75

Figure 3.

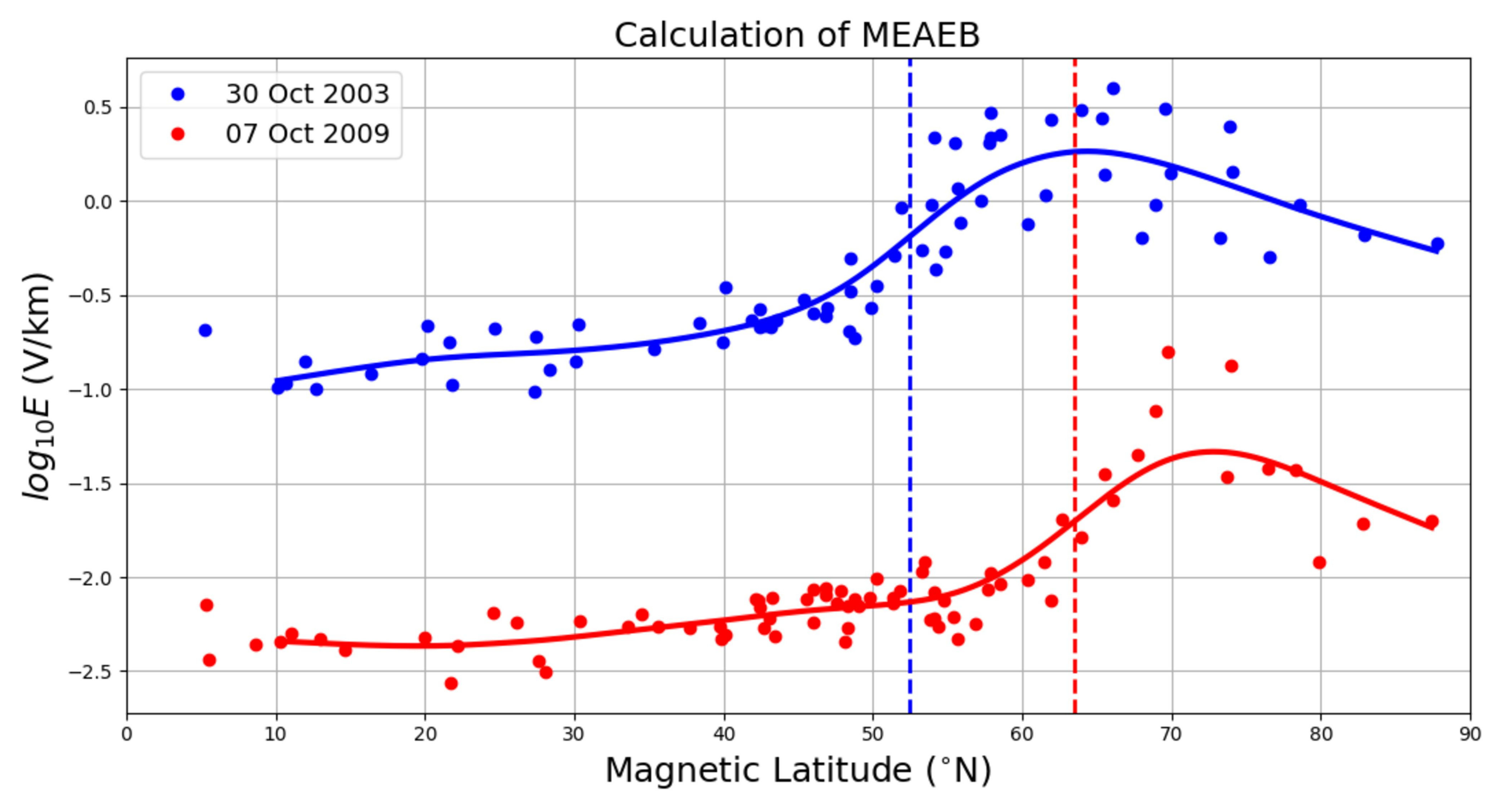

Calculation of MEAEB
30 Oct 2003
07 Oct 2009
0.5
0.0
-0.5
-1.0
-1.5
-2.0
-2.5
$log_{10}E$ (V/km)
0
10
20
30
40
50
60
70
80
90
Magnetic Latitude (°N)

Figure 4.

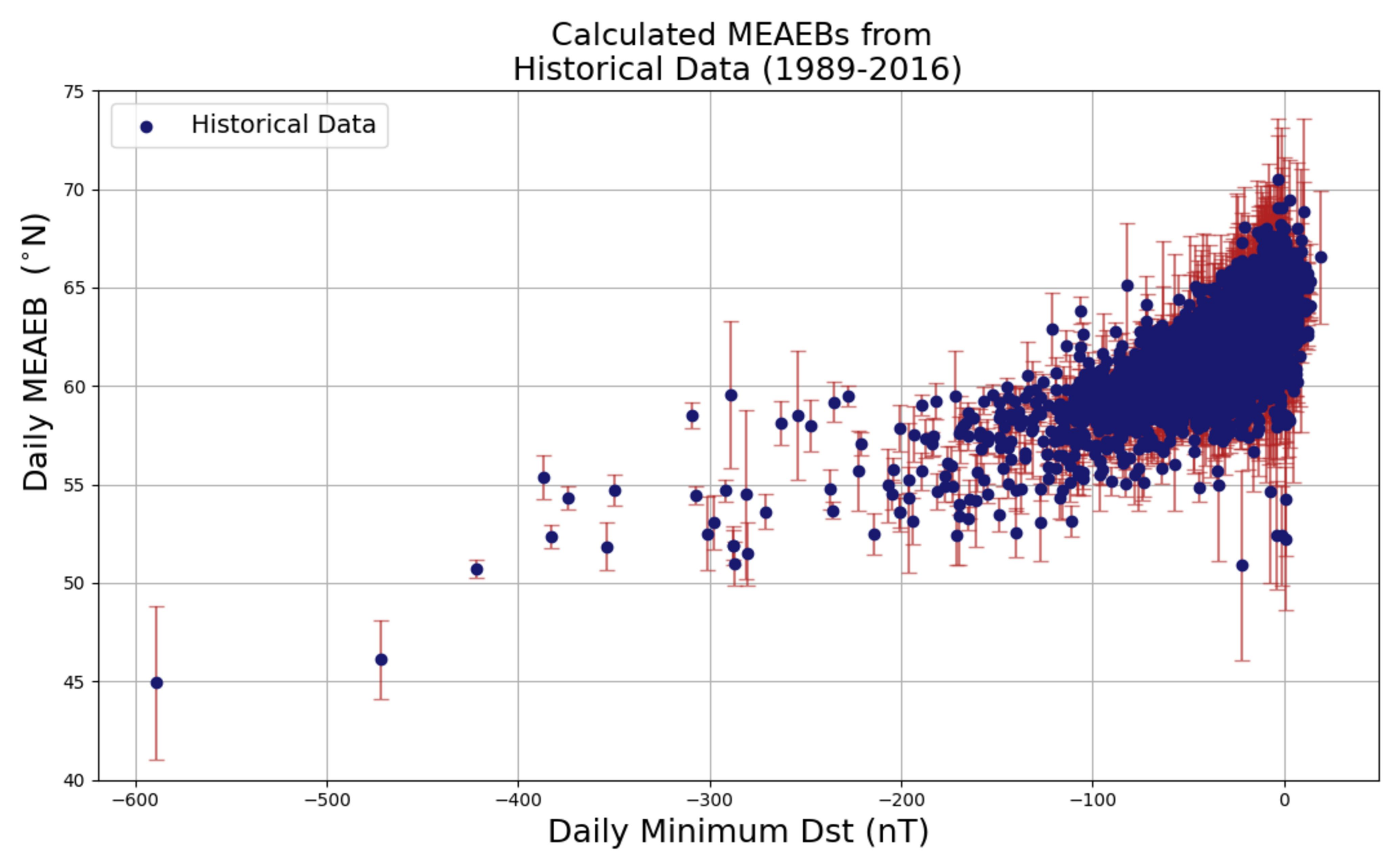

Calculated MEAEBs from
Historical Data (1989-2016)
Historical Data
Daily MEAEB (°N)
Daily Minimum Dst (nT)
75
70
65
60
55
50
45
40
−600
−500
−400
−300
−200
−100
0

Figure 5.

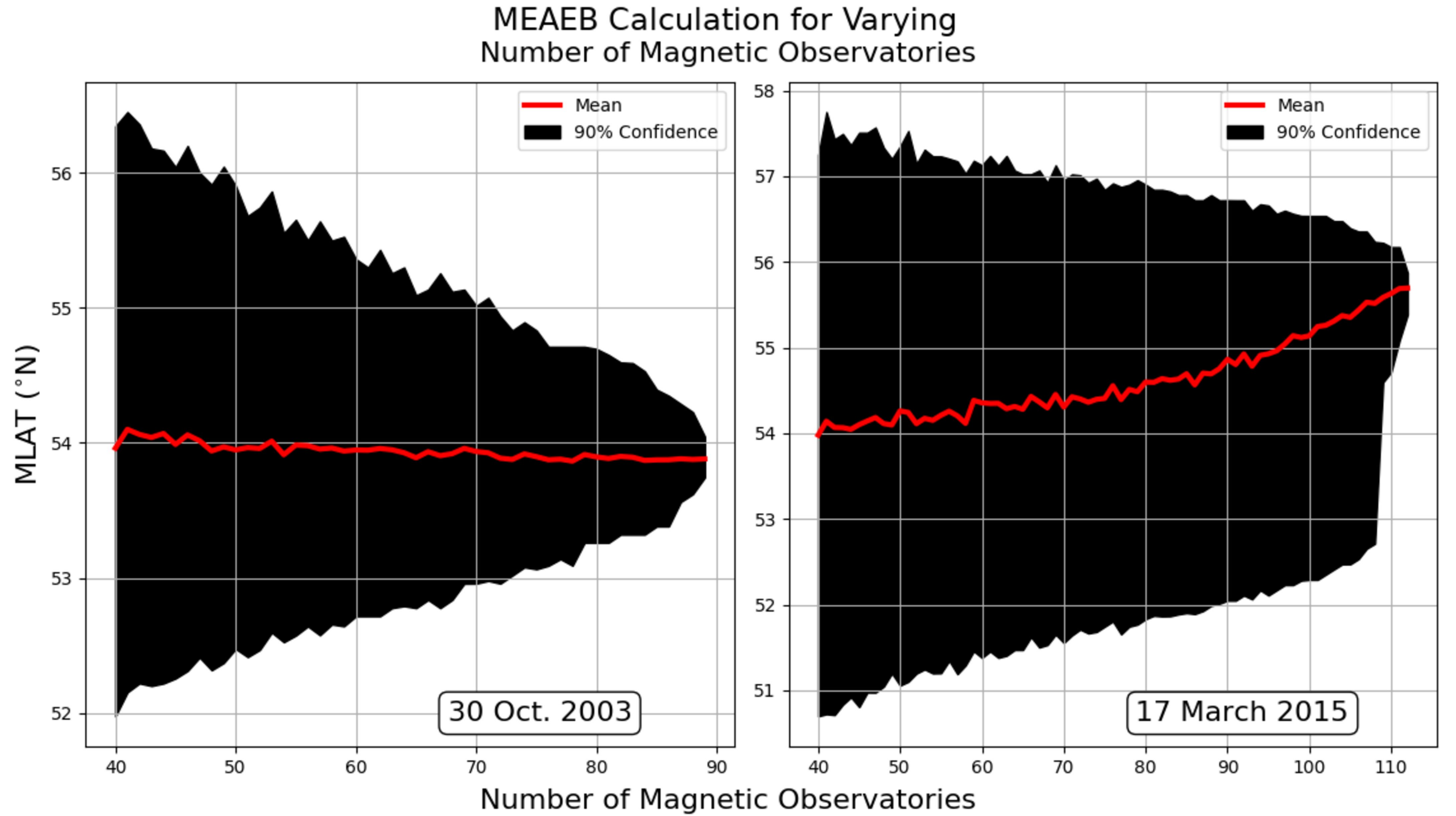

MEAEB Calculation for Varying
Number of Magnetic Observatories
MLAT (°N)
Number of Magnetic Observatories
Mean
90% Confidence
30 Oct. 2003
17 March 2015
52
53
54
55
56
57
58
51
40
50
60
70
80
90
100
110

Figure 6.

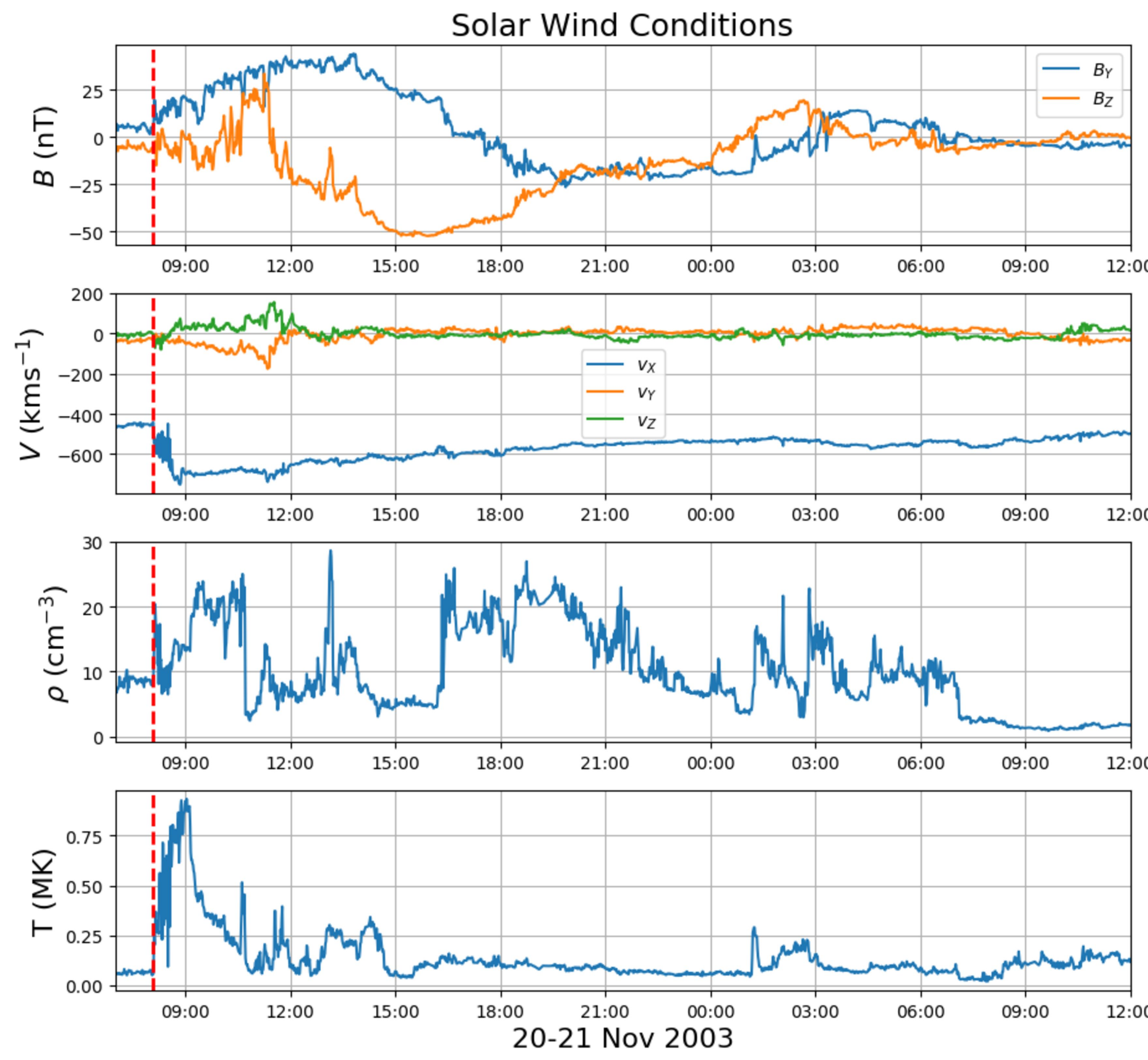

Solar Wind Conditions
B (nT)
B_Y
B_Z
V (kms^-1)
v_X
v_Y
v_Z
ρ (cm^-3)
T (MK)
09:00
12:00
15:00
18:00
21:00
00:00
03:00
06:00
09:00
12:00
20-21 Nov 2003

Figure 7.

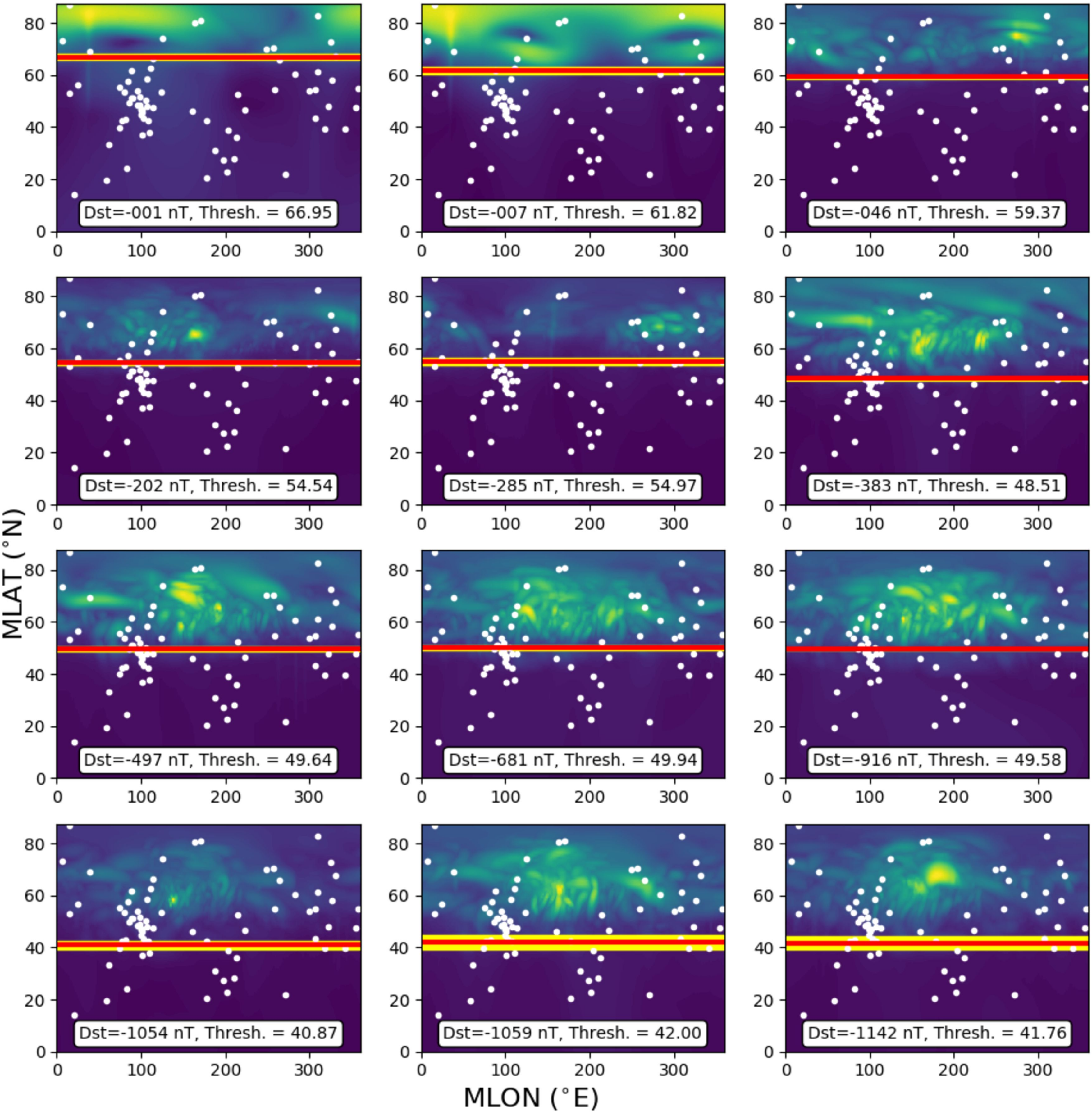

Dst=-001 nT, Thresh. = 66.95
Dst=-007 nT, Thresh. = 61.82
Dst=-046 nT, Thresh. = 59.37
Dst=-202 nT, Thresh. = 54.54
Dst=-285 nT, Thresh. = 54.97
Dst=-383 nT, Thresh. = 48.51
Dst=-497 nT, Thresh. = 49.64
Dst=-681 nT, Thresh. = 49.94
Dst=-916 nT, Thresh. = 49.58
Dst=-1054 nT, Thresh. = 40.87
Dst=-1059 nT, Thresh. = 42.00
Dst=-1142 nT, Thresh. = 41.76
MLAT (°N)
MLON (°E)

Figure 8.

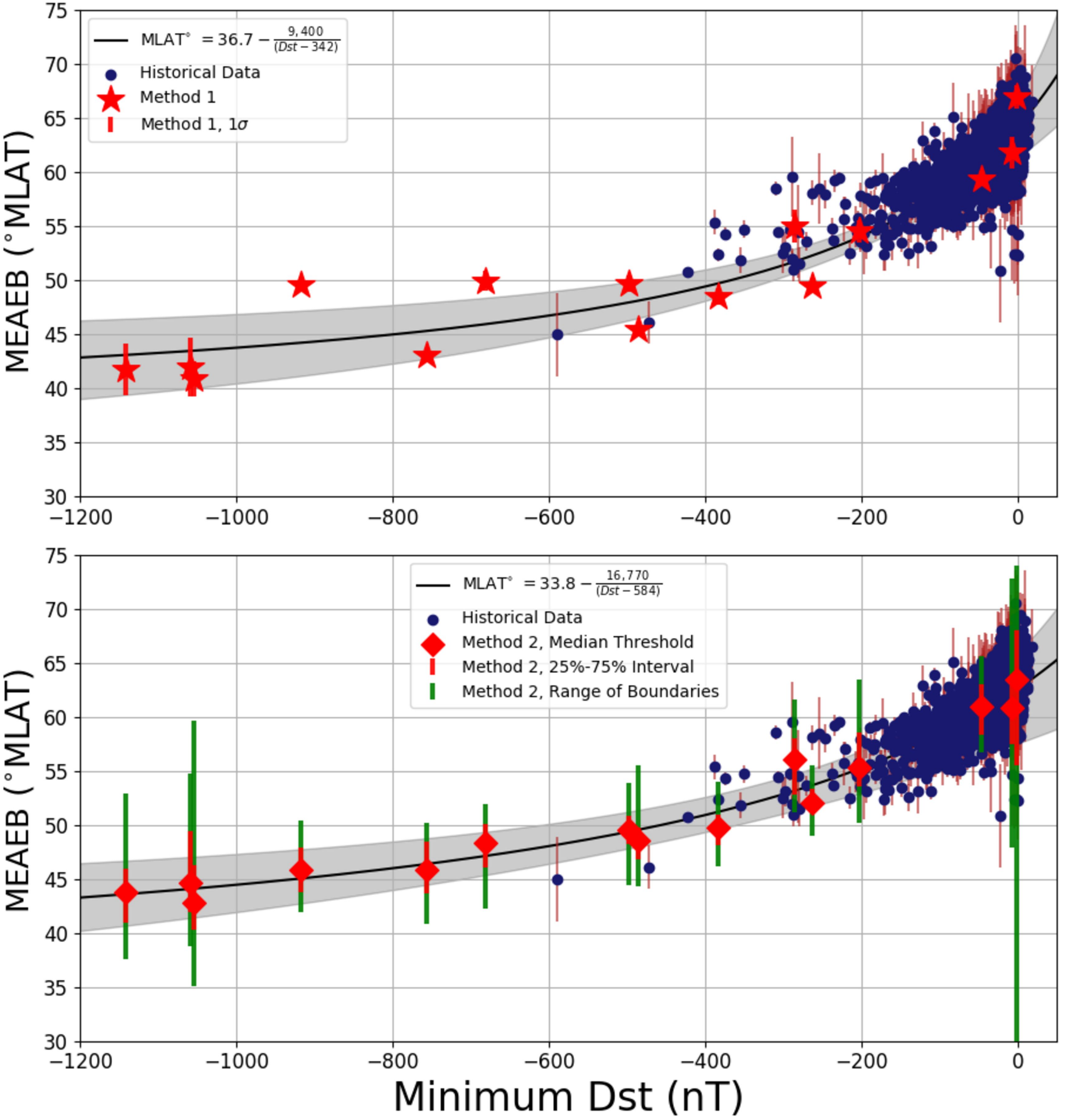

MLAT° $= 36.7 - \frac{9,400}{(Dst - 342)}$
Historical Data
Method 1
Method 1, 1σ
MEAEB (°MLAT)
MLAT° $= 33.8 - \frac{16,770}{(Dst - 584)}$
Historical Data
Method 2, Median Threshold
Method 2, 25%-75% Interval
Method 2, Range of Boundaries
MEAEB (°MLAT)
Minimum Dst (nT)

Figure 9.

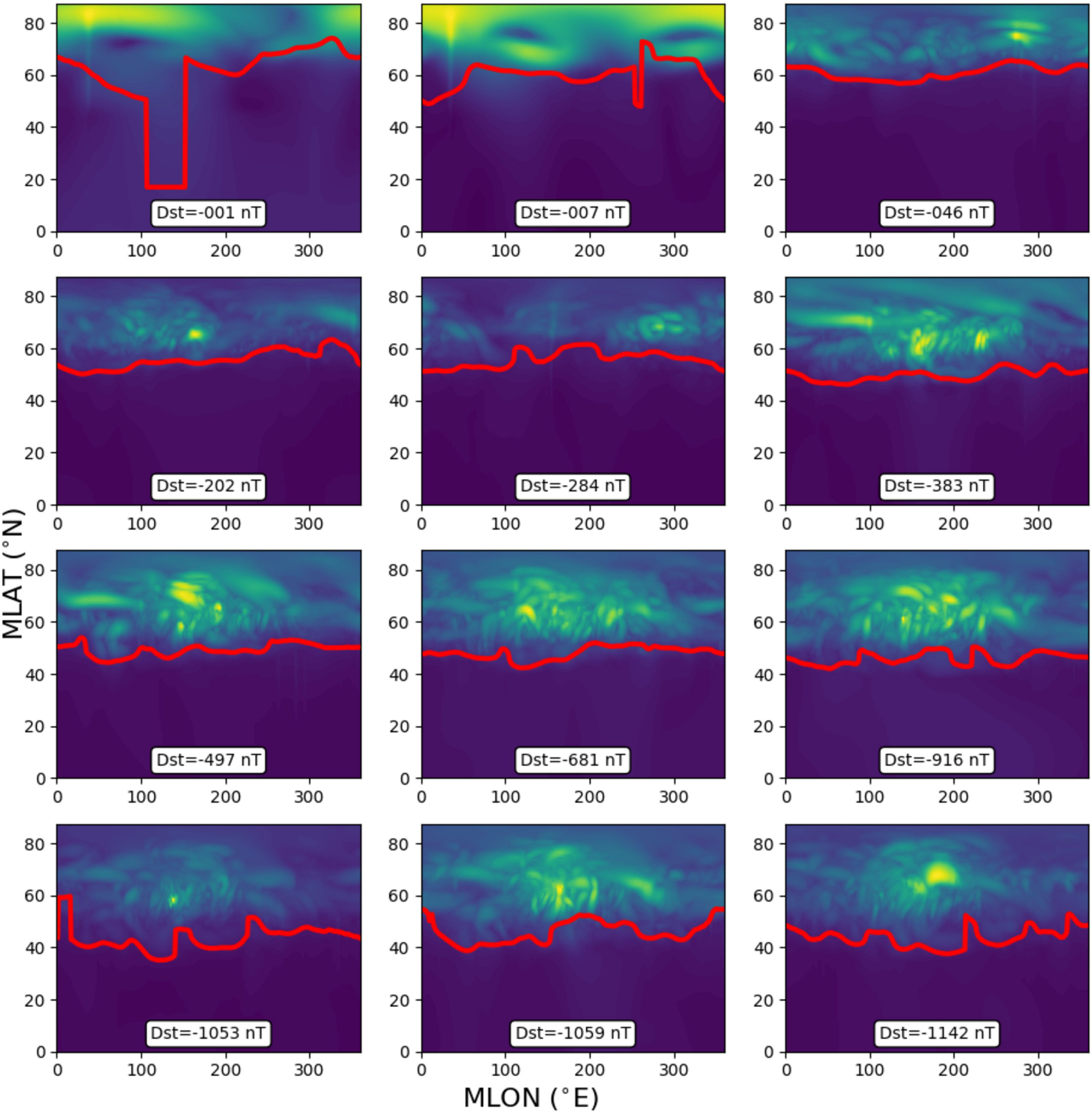

Dst=-001 nT
Dst=-007 nT
Dst=-046 nT
Dst=-202 nT
Dst=-284 nT
Dst=-383 nT
Dst=-497 nT
Dst=-681 nT
Dst=-916 nT
Dst=-1053 nT
Dst=-1059 nT
Dst=-1142 nT
MLAT (°N)
MLON (°E)

Figure 10.

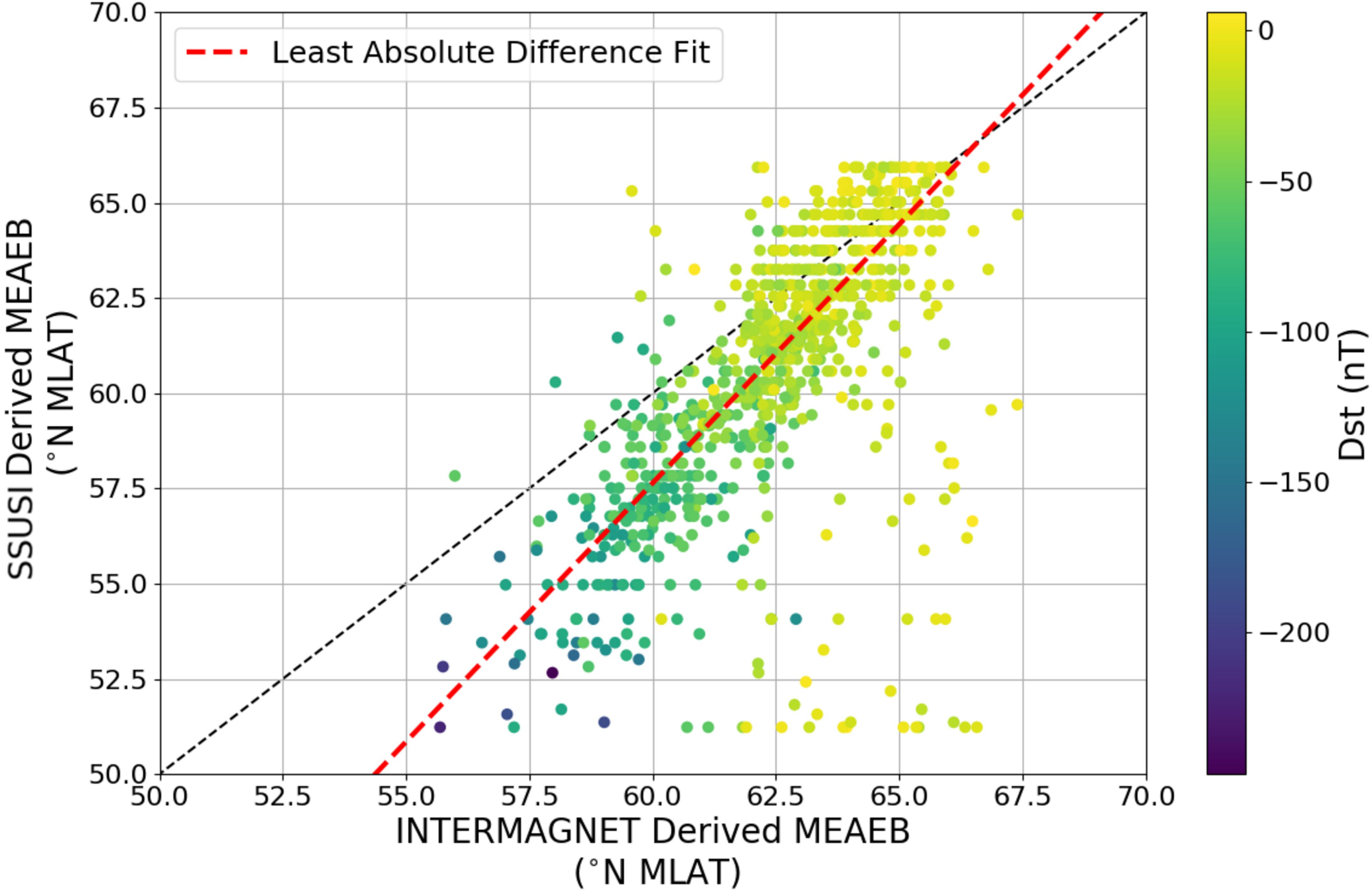

Least Absolute Difference Fit
SSUSI Derived MEAEB
(°N MLAT)
INTERMAGNET Derived MEAEB
(°N MLAT)
Dst (nT)
70.0
67.5
65.0
62.5
60.0
57.5
55.0
52.5
50.0
0
−50
−100
−150
−200

Figure 11.

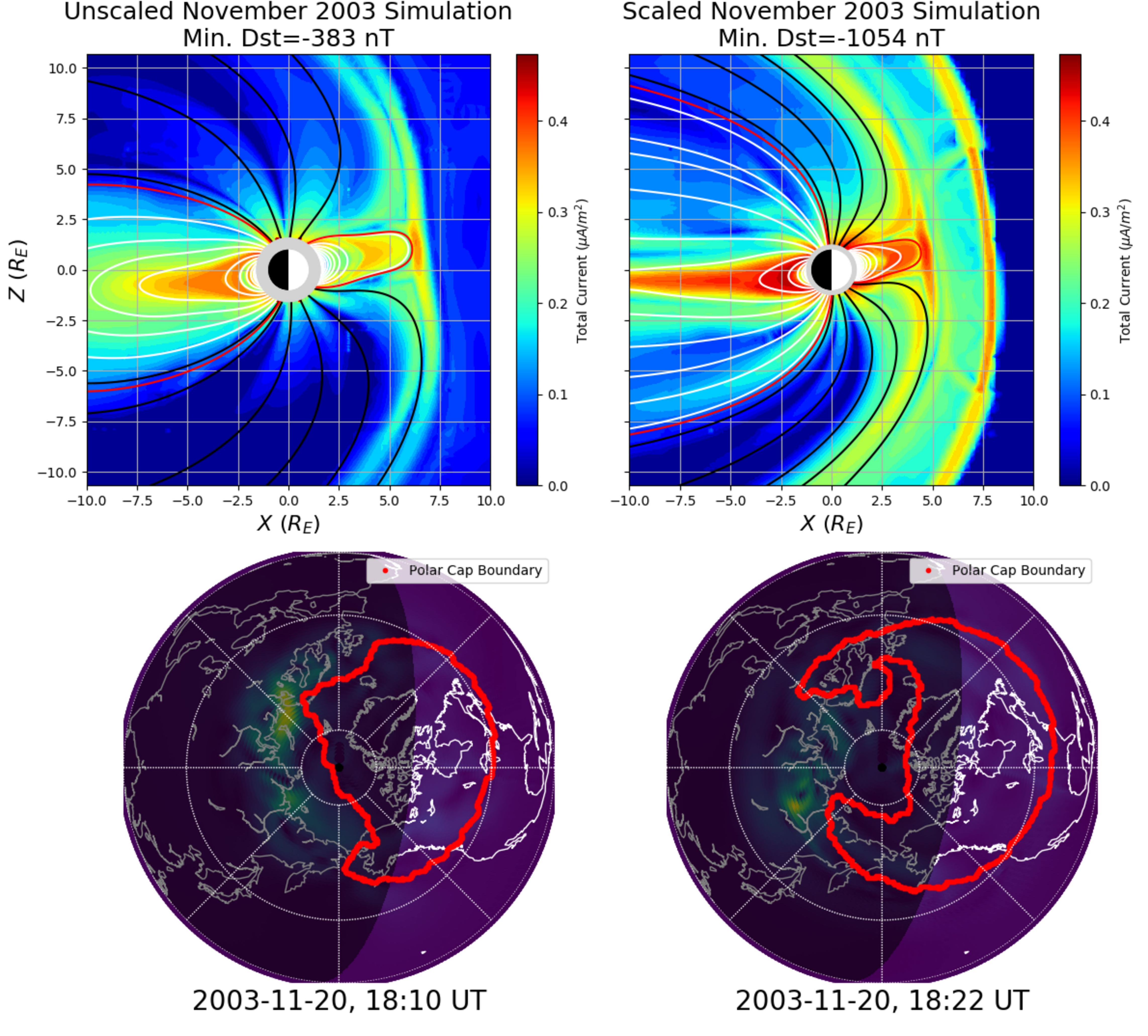

Unscaled November 2003 Simulation
Min. Dst=-383 nT
Scaled November 2003 Simulation
Min. Dst=-1054 nT
Z (R_E)
X (R_E)
Total Current ($\mu A/m^2$)
Polar Cap Boundary
2003-11-20, 18:10 UT
2003-11-20, 18:22 UT

Figure 12.

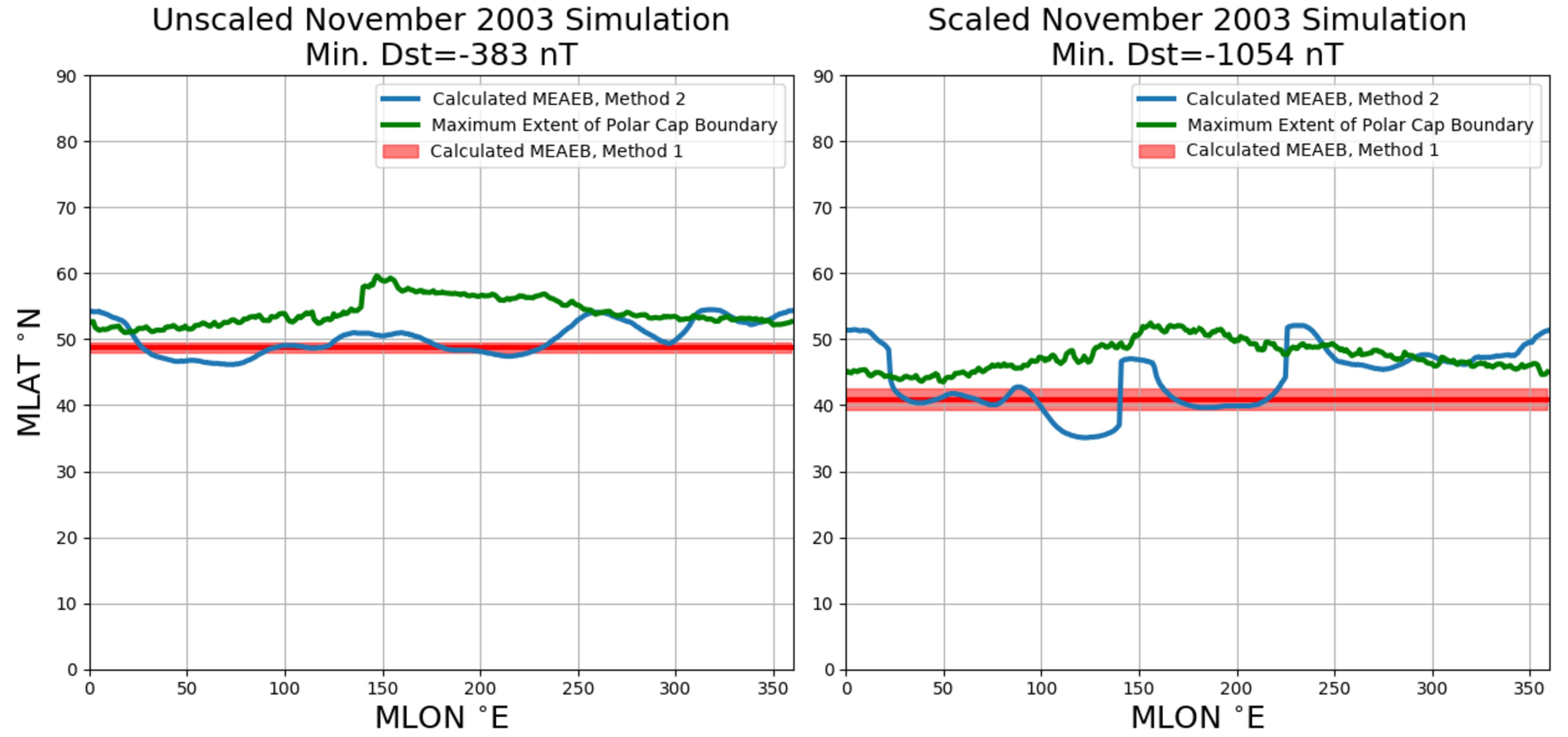

Unscaled November 2003 Simulation
Min. Dst=-383 nT
Scaled November 2003 Simulation
Min. Dst=-1054 nT
Calculated MEAEB, Method 2
Maximum Extent of Polar Cap Boundary
Calculated MEAEB, Method 1
MLAT °N
MLON °E

Figure 13.

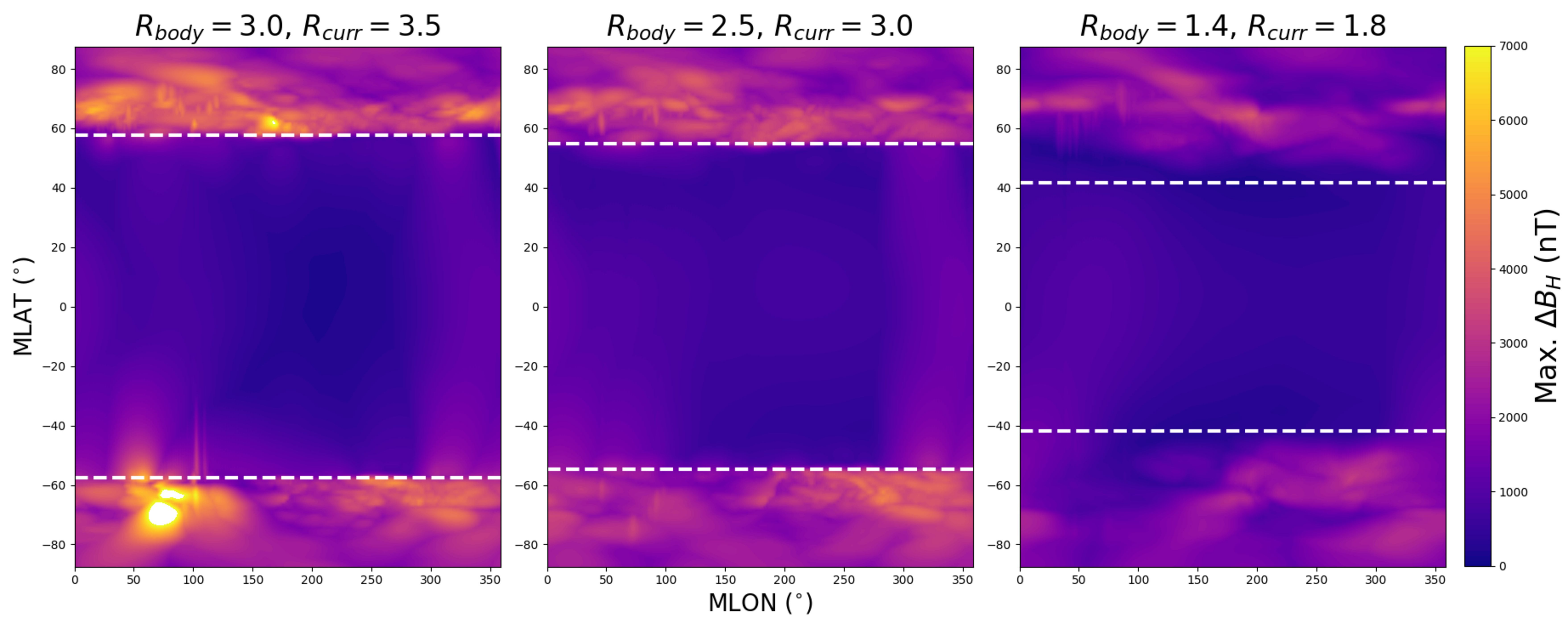
$R_{body} = 3.0$, $R_{curr} = 3.5$
$R_{body} = 2.5$, $R_{curr} = 3.0$
$R_{body} = 1.4$, $R_{curr} = 1.8$
MLAT (°)
MLON (°)
Max. ΔB_H (nT)
80
60
40
20
0
−20
−40
−60
−80
0
50
100
150
200
250
300
350
7000
6000
5000
4000
3000
2000
1000
0